WFIRST-AFTA Technical Report
Doc #: WFIRST-STScI-TR1503
Rev : A
Date : May 27, 2015

Data Post Processing and Algorithm Development for the WFIRST-AFTA Coronagraph: First Progress Report

PI: R. Soummer

M. Ygouf, L. Pueyo, M. Perrin

Space Telescope Science Institute (STScI)

3700 San Martin Dr, Baltimore, MD 21218

Context:

This technical report from Space Telescope Science Institute is associated to the AFTA-Coronagraph Data Post-Processing Algorithm subcontract No.1506553 led by the Jet Propulsion Laboratory (JPL). It represents the deliverable of the Milestone # 1 defined as follows: ”Provide interim evaluation of existing post-processing algorithms performance against simulated multi-wavelength data. Quantify the contrast gain expected from post-processing, as a function of angular separation”.

Contents

ABSTRACT

This technical report investigates post-processing techniques for high-contrast imaging in the context of WFIRST-AFTA. It represents the deliverable of the Milestone # 1 of the post-processing effort led by JPL defined as follows: "Provide interim evaluation of existing post-processing algorithms performance against simulated multi-wavelength data. Quantify the contrast gain expected from post-processing, as a function of angular separation".

In order to gain insight into post-processing performance at very-high contrast, we studied three techniques of PSF subtraction on simulated temporal and multi-spectral data to evaluate their performances in term of contrast gain as a function of angular separation: the classical PSF subtraction, the Karhunen-Loève Image Projection (KLIP) and the classical spectral deconvolution (SD) techniques. This work quantifies the relative contrast gain provided by post-processing under various assumptions for spacecraft+telescope+instrument thermal models and observing scenarios. It is by no means a reflection upon the validity of these models in terms of absolute contrast.

We found that the performances of PSF subtraction techniques depends on the stability and the amount of the aberrations. In a case where the aberrations are quite stable, the classical PSF subtraction and KLIP techniques lead to similar levels of contrasts. But if the temporal stability of aberrations decreases or the amount of aberrations increases, KLIP enables a better detection than the classical PSF subtraction. KLIP is therefore more robust than the classical PSF subtraction. We quantify the contrast gain expected from post-processing as a function of angular separation for each analysed data set. We also found that the classical spectral deconvolution technique is useless as is to reduce multi-spectral data in the context of WFIRST-AFTA: it is not possible to disentangle a planet signal from the speckles because the model of the speckles also fits the planet.

INTRODUCTION

HIGH-CONTRAST IMAGING WITH THE WFIRST-AFTA CORONAGRAPH

Direct imaging of exoplanets is a highly challenging technique as it requires to reach extreme values of contrast between the flux of a planet and its host star. For the WFIRST-AFTA coronagraph the contrast requirement is 10^{-9} [1]. It is planned to reach contrasts of about 10^{-8}, using state-of-the-art starlight suppression and wavefront control techniques. As part of the star-light suppression, two different kind of coronagraphs have been selected for the mission:

a shaped-pupil coronagraph (SPC), which is based on an optimal binary apodizer [2, 3, 4] and a hybrid lyot coronagraph (HLC) [5, 6]. In this report, we reduce and analyze data sets simulated with these two coronagraphs [7]. A system of two deformable mirrors (DMs) is used to control the wavefront upstream of the coronagraph to correct the wavefront in real time, creating the characteristic dark-holes in the focal plane with the help of an Electric Field Conjugation (EFC) algorithm [8]. A Low Order WaveFront Sensing and Control LOWFSC subsystem uses the starlight that is rejected by the coronagraph to measure low-order aberrations caused by the pointing jitter of the telescope or thermal variations [9]. Finally, a ten-fold contrast improvement to reach the required contrast of 10^{-9} to image and characterize reflected-light gas giants with WFIRST-AFTA is expected to come from post-processing. But the methods of point spread function (PSF) subtraction techniques currently used on both ground-based and space-based instruments have not yet been demonstrated at such high contrast level. The goal of this document is to report our investigation about post-processing techniques on high-contrast multi-spectral data with synthetic planets.

OBSERVING STRATEGIES WITH WFIRST-AFTA AND ASSOCIATED PSF SUBTRACTION TECHNIQUES

Depending on the observation strategy, different PSF subtraction techniques can be used to reduce high-contrast imaging data. In the case of WFIRST-AFTA, an example observing scenario requiring the consecutive observation of three different stars has been designed: a bright star is targeted (beta Uma (A1IV, V=2.37)) for the dark hole generation; it is then the science target's turn (47 Uma (G1V, V=5.04)) to be observed; finally a calibration star (61 Uma (G8V, V=5.34)) is observed as a reference PSF. With such an observation strategy, also called reference star differential imaging (RDI) [10], we can think about using two different kinds of data reduction methods.

The classical PSF subtraction can be seen as one of the simplest methods of post-processing used to subtract the highly problematic speckles from a high-contrast image. This technique consists of imaging a reference image to calibrate the PSF in the focal plane and subtracting it from the image of the target star. This technique has been used extensively to detect disks in direct imaging. Very simple to implement, we apply it systematically as a reference method in this report.

The Locally Optimized Combination of Images (LOCI) [11] algorithm and the Principal Component Analysis (PCA) method [12, 13], also based on RDI, perform linear combinations of a library of reference PSFs. These methods produce similar results in terms of PSF subtraction [12]. Moreover, with the PCA method, which is also called KLIP for Karhunen-Loève Image Projection, one knows how to alleviate the biases in the astrometry and photometry which are usually associated with LOCI-based PSF subtractions schemes [12]. For this reason, we choose to focus on applying KLIP to reduce the data in this report. The KLIP method decom-

poses in principal components a library of PSFs free of astrophysical signal. The science target is then projected into those principal components to create a synthetic reference, which is subtracted from the target. This method has been implemented to process images of NICMOS and WFC3 data of the HR8799 planetary system [12, 14]. It is currently implemented in the ALICE pipeline, which will reprocess the HST-NICMOS archive [15, 16] as well as the post-processing method for ground-based instrument images such as P1640 [17], GPI [18], SPHERE [19] and NaCo [20]. The first part of this report focuses on the techniques using RDI.

We can also think about using the spectral diversity offered by the integral field spectrograph (IFS) of WFIRST-AFTA. In the second part of this report, we particularly study the ”so-called” Spectral Deconvolution (SD) technique. This method, which takes advantage of the chromatic behavior of the coronagraphic PSF to disentangle the signal of a planet from the speckles, has been applied successfully for different simulated and real images in different contexts. Sparks and Ford introduced and validated the concept on simulated data [21]. Thatte et al. applied the method to real ground-based AO-assisted IFS data sets from the SINFONI instrument [22] on the Very Large Telescope (VLT). The spectral deconvolution technique is currently used as a baseline for spectrum extraction in the SPHERE instrument pipeline [23] and some studies focus on further developments in the context of the future planet imager for the European-Extremely Large Telescope (E-ELT) [24, 25].

I REFERENCE DIVERSITY

In this first part, we focus on exploiting the reference diversity enabled by the observing scenario described in the introduction, applying the classical PSF subtraction and the KLIP techniques on data sets received from JPL for two different observing scenarios (OS): OS1 and OS3. The first observing scenario assumes a geosynchronous orbit with thermal models corresponding to the coronagraph design for the cycle 4. The observing scenario 3 assumes the same geosynchronous orbit as for OS1 but without the Earth effects. It corresponds to the coronagraph design for the cycle 6 and thus simulates different thermal effects from OS1. Two different data sets are provided for this observing scenario, simulating images with and without the LOWFC system. In section 1, we first describe the broadband OS1 time series data simulated with a Hybrid Lyot Coronagraph (HLC) before reducing and analysing them. In section 2, we perform a statistical analysis of the raw data sets, in an attempt to better understand our observations. In section 3, we describe, reduce and analyze the broadband OS1 time series data simulated with a Shaped Pupil Coronagraph (SPC). Finally in section 4, we perform the same steps for the broadband OS3 time series data simulated with a Hybrid BandLimited Coronagraph (HBLC).

1 HLC OS1 TIME SERIES

This section covers our analysis of the simulated broadband HLC OS1 time series. We assess the applicability of the KLIP algorithm and compare its performance with the classical PSF subtraction on temporal data simulated with an HLC coronagraph for the observing scenario OS1. We also quantify how robust these methods are to increasing amounts of coma. We first describe the simulated data that STScI received from JPL in the sub-section 1.1, before reducing and analysing them in the sub-section 1.2. Sub-sub-section 1.2.1 focuses on the first set of data that we received (also called "initial distribution" in this report), whereas sub-sub-section 1.2.2 focuses on the second one with different amounts of coma.

1.1 DESCRIPTION OF SIMULATIONS

1.1.1 INITIAL DISTRIBUTION

A set of images was generated by John Krist for the WFIRST-AFTA OS1 observing scenario using the hybrid lyot coronagraph HLC 20140623-139 (10% bandpass, 550 nm, r = 2.6 λ/D spot, IWA ≈ 3 λ/D, OWA = 10.5). Two sets of images were simulated: 47 Uma as science target and beta Uma for the dark hole generation. The wavefront was optimized simultaneously for

the X and Y polarizations.

OS1 time series - John Krist, JPL - 23 October 2014

Noiseless data

OS1.0_47_Uma_HLC_polX_sequence_noiseless.fits

OS1.0_47_Uma_HLC_polY_sequence_noiseless.fits

OS1.0_beta_Uma_HLC_polX_sequence_noiseless.fits

OS1.0_beta_Uma_HLC_polY_sequence_noiseless.fits

Noisy data

OS1.0_47_Uma_HLC_polX_sequence.fits

OS1.0_47_Uma_HLC_polY_sequence.fits

OS1.0_beta_Uma_HLC_polX_sequence.fits

OS1.0_beta_Uma_HLC_polY_sequence.fits

1.1.2 COMA DISTRIBUTION

We received additional files as part of the OS1 time series distribution for the WFIRST-AFTA HLC OS1.0 scenario. They are noiseless data in the X polarization channel with the wavefront optimized for that channel.

OS1.0 time series with different amounts of coma - John Krist, JPL - 3 Feb 2015

beta and 47 Uma OS1.0 sequences with the default aberrations (1x coma plus the other aberrations) to go along with the previous distribution). 47 Uma sequences provided with and without planets:

OS1.0_beta_Uma_HLC_polX_sequence_noiseless.fits

OS1.0_47_Uma_HLC_polX_sequence_noiseless.fits

OS1.0_47_Uma_HLC_polX_sequence_noiseless_no_planets.fits

47 Uma OS1.0 sequence with planets, without noise, and having 2x or 4x the default amount of coma (other aberrations unaltered):

OS1.0_47_Uma_HLC_polX_coma2x_sequence_noiseless.fits

OS1.0_47_Uma_HLC_polX_coma4x_sequence_noiseless.fits

OS1.0_47_Uma_HLC_polX_coma2x_sequence_noiseless_no_planets.fits

OS1.0_47_Uma_HLC_polX_coma4x_sequence_noiseless_no_planets.fits

Beta Uma OS1.0 sequence (bright star for dark hole acquisition, no planets), without noise, and having 2x or 4x the default amount of coma (other aberrations unaltered):

OS1.0_beta_Uma_HLC_polX_coma2x_sequence_noiseless.fits

OS1.0_beta_Uma_HLC_polX_coma4x_sequence_noiseless.fits

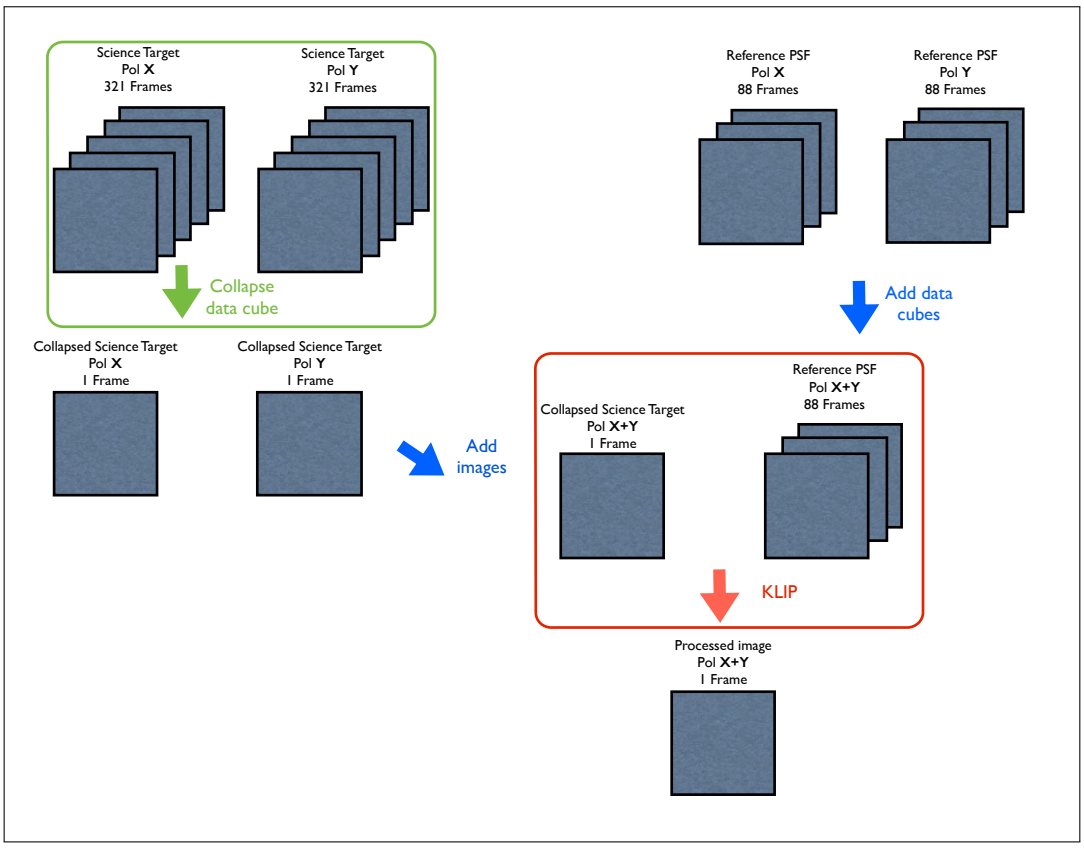

Figure 1: Illustration of the reduction steps with KLIP

1.2 POST-PROCESSING AND ANALYSIS OF THE DATA

1.2.1 OS1 TIME SERIES, INITIAL DISTRIBUTION

Post-processing. Before reducing the data with KLIP, we collapse the science data cubes (47 Uma) for the polarizations X and Y to obtain two long exposure raw images (the collapsed science target in the polarization X and the collapsed science target in the polarization Y). We then take the sum of these two images to form what we call the collapsed science target. The KLIP library is then built using the reference PSF data cubes in the polarization X and Y. These two cubes are co-added before being decomposed in principal components through the KLIP algorithm. This reduction process is illustrated in figure 1.

The figure 2 shows the results of the reductions for noiseless and noisy data. We represented on the same dynamic the long exposure raw science data cube (all slices collapsed), the classical PSF subtraction reduction and the KLIP reduction with 4 and 88 modes.

Analysis. The two techniques show a relatively good PSF subtraction compared to the raw image for both noiseless and noisy cases. Four planet candidates can be identified with numbers 1, 2, 3 and 4 (cf. Figure 3). For the noiseless data set, two planets were detected with the two methods (candidates #1 and #2). One candidate (candidate #3) was discarded because of its position being too close to the star. It has not been possible to conclude for the another candidate (candidate #4) with either one or the other technique. Quantitative metrics for de-

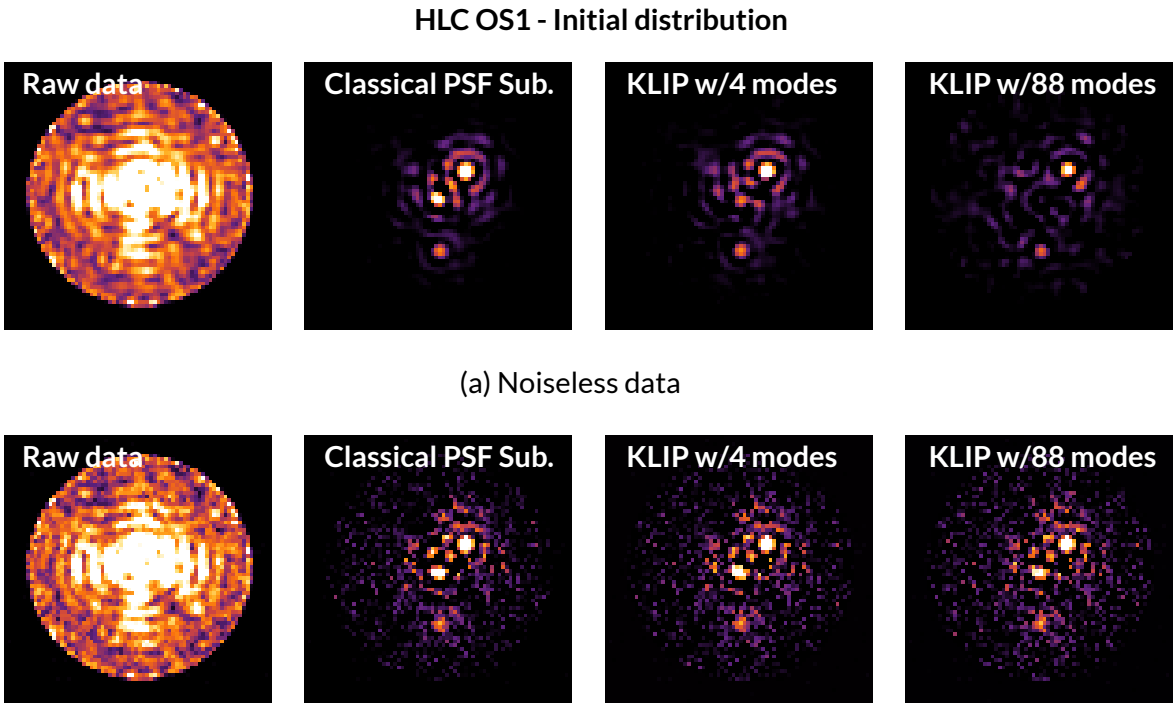

(a) Noiseless data

(b) Noisy data

Figure 2: **HLC OS1 time series - Initial distribution**. Comparison of the raw data and three different reductions. Top: (a) noiseless data. Bottom: (b) noisy data. From left to right with same dynamic range: raw image (long exposure), image processed with classical PSF subtraction, image processed with KLIP 4 modes and image processed with KLIP 88 modes. The two techniques show a relatively good and similar PSF subtraction compared to the raw image.

tection will be developed further into the project (cf. section 7).

If we have a closer look at the noisy case on the bottom of the figure 2, there seems to be no difference between the three reductions. Without any surprise, the detection is more difficult in the noisy case. We can still identify two planet candidates (candidates #1 and #2) but the candidate #3 is not longer detectable.

We represent the contrast gain as a function of separation for the different reductions in the figures 4 and 5 for the noiseless and noisy data respectively. These curves do not take into account the throughput of KLIP. The contrast gains with KLIP are therefore a little bit optimistic here.

Other studies have also been done by us in the context of this particular data set. For the sake of clarity, we only report the studies that are the most relevant to quantify the contrast gain expected from post-processing. Two other studies are reported in appendix 10 and 11.

To conclude on this data set, the contrast improvements are quite similar in the different reductions with both KLIP and the classical PSF subtraction. The thermal model in OS1 seems to lead to a very stable wavefront and under these very stable conditions, we could think about using both reduction strategies, i.e. classical PSF subtraction as well as KLIP. In the case of noisy data the differences between the two reduction methods are even smaller than in the case of noiseless data set. We further address the issue of KLIP performance with respect to classical

PSF subtraction for this particular set of data in section 2.

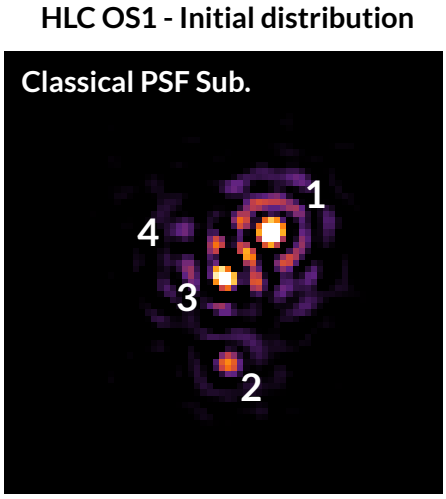

Figure 3: **HLC OS1 time series - Initial distribution.** Planet candidates identified in the classical PSF reduction for the noiseless case. The planet candidates #1 and #2 are well detected. The current analysis of this data set does not enable to confirm the presence of a third or fourth planet.

1.2.2 OS1 TIME SERIES WITH DIFFERENT AMOUNTS OF COMA

Before reducing the data with KLIP for the case with different amounts of coma, we perform exactly the same preparatory processing of the data as for the initial distribution (cf. section 1.2 and Figure 1), except that we have only the X polarization for this data set.

By reducing both initial and coma distributions, we noticed a difference in the results. Indeed, the raw contrast is better in the coma distribution. While the thermal model is the same in the two distributions, the wavefront control strategy with respect to the polarization is different (see the associated reduction results and detailed discussion in appendix 12). This leads to the identification of the planet candidate 4b instead of 4 in the initial distribution (cf. Figure 7).

We compare in the figure 6 the reduction results for different amounts of coma. The classical PSF subtraction reduction, as well as the KLIP reduction with 4 and 88 modes show a relatively good PSF subtraction compared to the raw image for the different amount of coma. But on the contrary to the case with the reference amount of coma, KLIP with 88 modes does a better job as cleaning the residual speckles when the amount coma is higher. The case of coma multiplied by 4 is the more explicit as the KLIP reduction with 88 is the only one which enables the detection of the two same candidates identified previously (candidates #1 and #2).

We represent the contrast gain as a function of separation for the different reductions in the figure 8. These curves do not take into account the throughput of KLIP. The contrast gains with KLIP is therefore a little bit optimistic here. The gain with KLIP increases when the amount of coma increases contrary to the gain with the classical PSF subtraction, which decreases when the amount of coma increases.

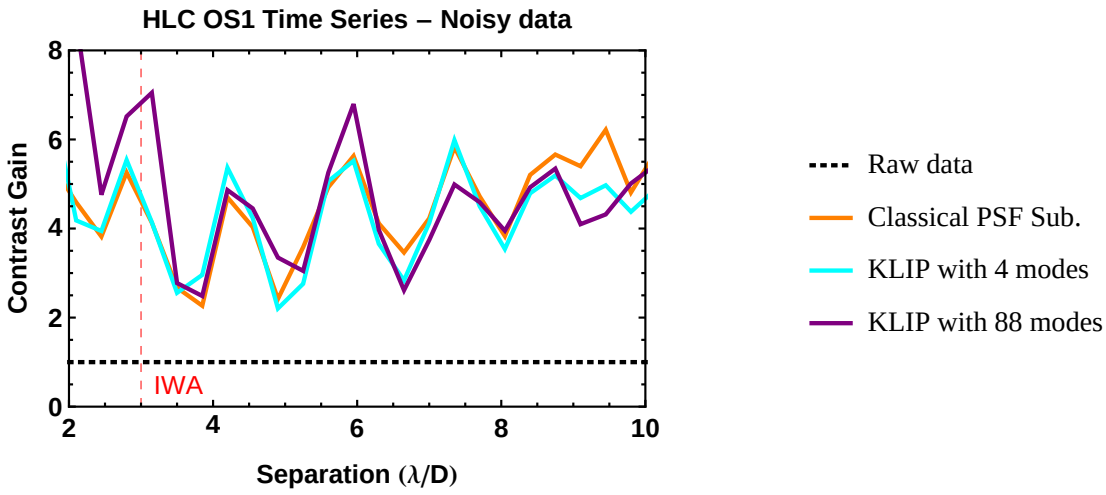

Figure 4: **HLC OS1 time series - Initial distribution.** Contrast gain as a function of separation for noiseless data. These curves do not take into account the throughput of KLIP. The three reductions show similar contrast gains.

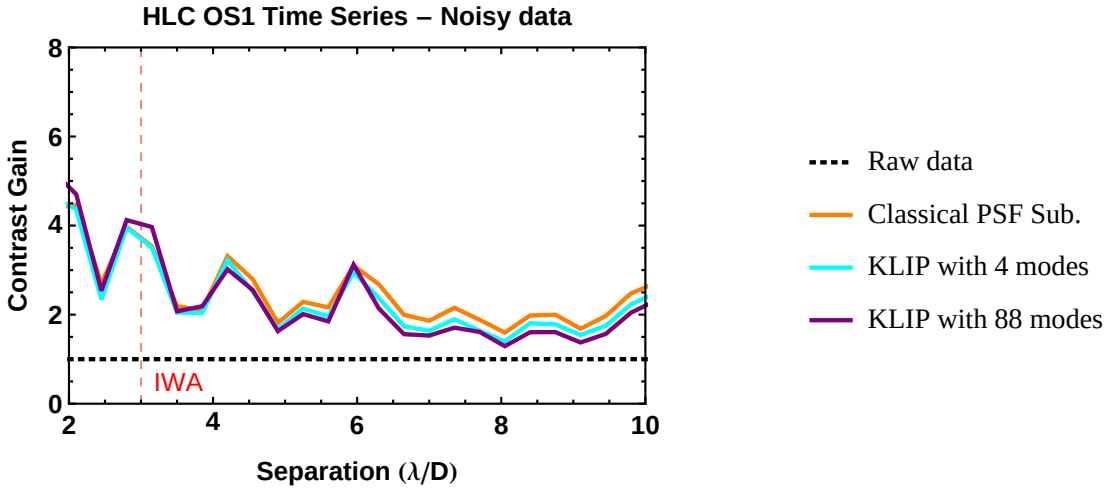

Figure 5: **HLC OS1 time series - Initial distribution.** Contrast gain as a function of separation for noisy data. These curves do not take into account the throughput of KLIP. The three reductions show similar contrast gains.

To conclude on this data set, KLIP performs better than the classical PSF subtraction with higher levels of coma, enabling to detect the candidates #1 and #2 even with an amount of coma multiplied by 4. The contrast gain is better with KLIP (multiplied by 3 with respect to the classical PSF subtraction for coma x4 with 88 KLIP modes). Even though the thermal model used for the simulations is the same as for the initial distribution, the classical PSF subtraction is more sensitive than KLIP to bigger amounts of aberrations. More conclusions about this data set can be found in section 2.

2 CORRELATION STUDY FOR BOTH WFIRST-AFTA-LIKE SIMULATED DATA AND HST DATA

The post-processing results of the OS1 data showed that KLIP does not perform better than the classical PSF subtraction. In this section we perform a statistical analysis of the OS1 raw

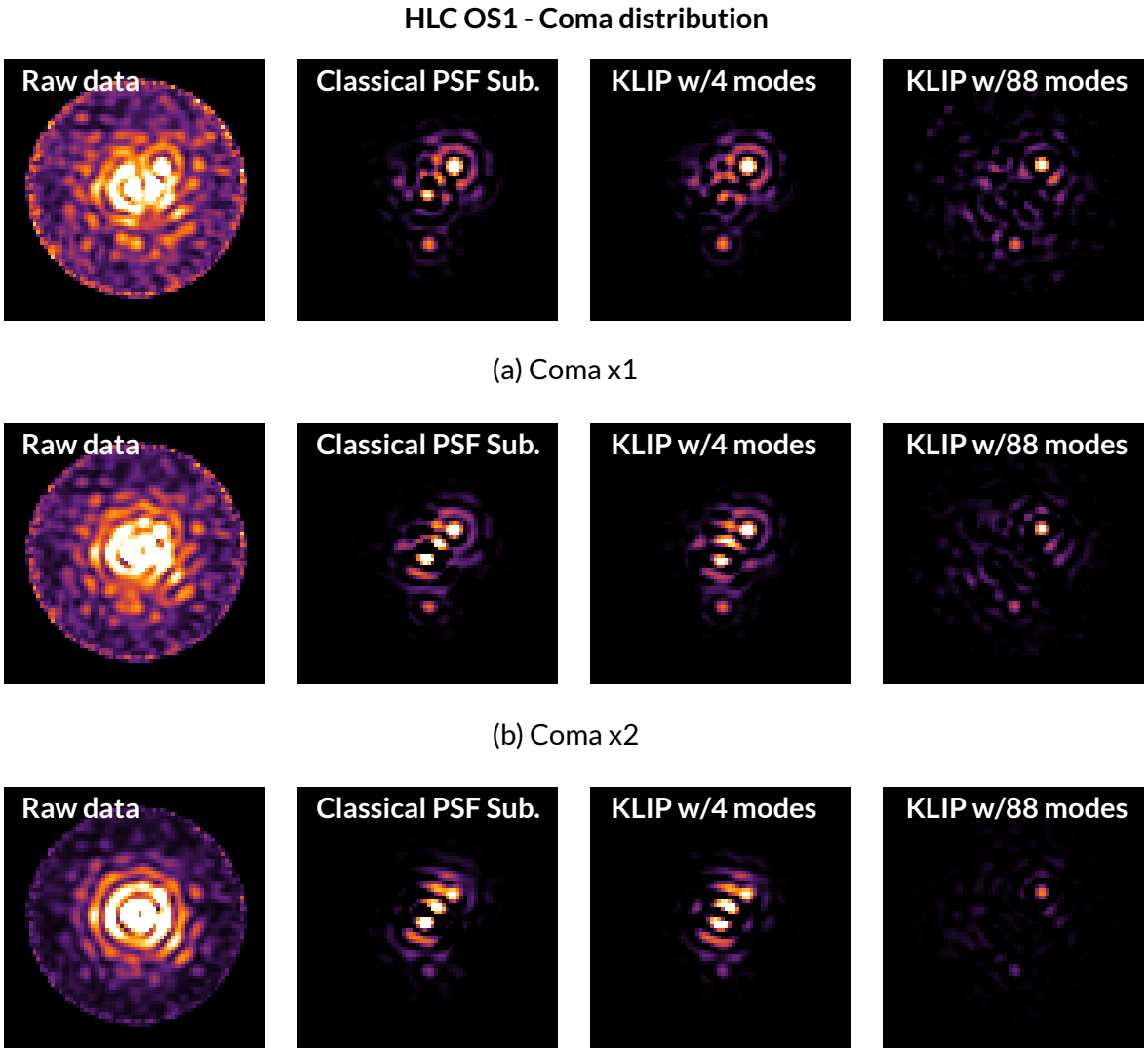

Figure 6: **HLC OS1 time series - Coma distribution.** Comparison of the raw data and three different reductions for different amounts of coma. Top: (a) coma x1 (reference amount). Middle: (b) coma x2. Bottom: (c) coma x4. From left to right with same dynamic range: raw image (long exposure), image processed with classical PSF subtraction, image processed with KLIP 4 modes and image processed with KLIP 88 modes. Whereas the two techniques show a relatively good and similar PSF subtraction compared to the raw image for the reference amount of coma (coma x1), KLIP with 88 modes performs better than the classical PSF subtraction when the amount of coma increases.

data as well as some HST-NICMOS data for which KLIP gives better results than the classical PSF subtraction to investigate the reasons of this unusual observation.

2.1 DESCRIPTION OF COMPUTATIONS

We computed the cross-correlations of the first slice of the 47 Uma (target) data cube with each slice of the beta Uma (reference) data cube of the OS1 time series (cf. sub-section 1.1 for

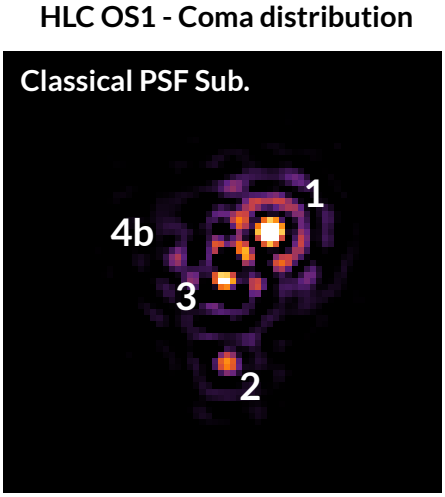

Figure 7: **HLC OS1 time series - Coma distribution.** Planet candidates identified in the coma distribution in the classical PSF reduction for the noiseless case. The planet candidates #1 and #2 are well detected. The current analysis of this data set does not enable to confirm the presence of a third or fourth planet.

a description of the simulations).

$$C^i = \frac{1}{N} \sum_{x,y} \frac{\left[I_1^i(x,y) - \bar{I}_1^i\right] \left[I_2(x,y) - \bar{I}_2\right]}{\sigma_{I_1^i} \sigma_{I_2}}, \tag{1}$$

with I_1^i is the i-th of the reference data cube, I_2 is the first image of the target data cube, N is the total number of pixels in the images, $\sigma_{I_1^i}$ and σ_{I_2} are respectively the standard deviation of the images I_1^i and I_2. We plot the evolution of the correlation with respect to the number of the beta Uma slice for the intial (Figure 9) and the coma (Figure 11) distribution. Because each slice of the reference cube corresponds to the successive times at which the images were taken, the evolution of the correlation with the number i of the reference cube slice can also be seen as an evolution of the correlation with time. The plot shows that the correlation increases with time. This suggests that the test case simulates a reference data cube acquisition during a phase when the telescope is not stabilized. The corresponding histograms in the figures 10 and 12 shows the associated statistics.

We computed the same correlations for the HST-NICMOS data as for the OS1 case. The evolution of the correlation with time during reference acquisition is quite different from what we observe for the OS1 simulations. It corresponds clearly to a phase when the telescope is stabilized.

2.2 DISCUSSION

In section 1, we saw that the contrast improvements were similar with the KLIP and classical PSF subtraction techniques for the HLC OS1 time series data set. We made the same observation for both noiseless and noisy data, but the analysis conducted in this section shows that it is not for the same reason. In the case of noiseless data, the figure 9 shows a small increase

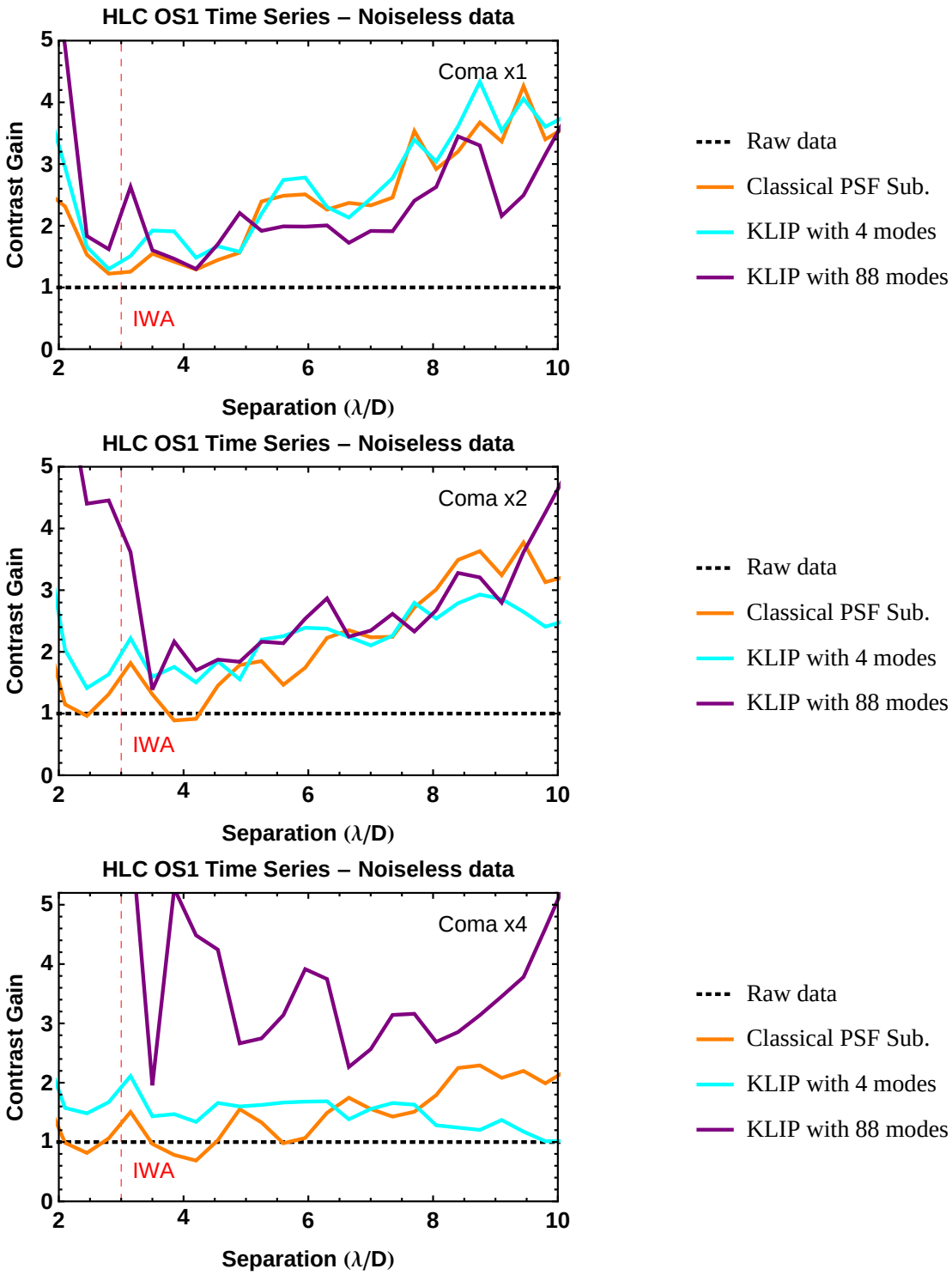

Figure 8: **HLC time series - Coma distribution.** Contrast gain as a function of separation for different amount of coma. These curves do not take into account the throughput of KLIP. The three reductions show similar contrast gains for the reference amount of coma (coma x1). KLIP with 88 modes shows a better contrat gain than the other reductions when the level of coma increases.

of the cross-correlations with time, indicating that the telescope was not stabilized during the acquisition of the reference star images. But the wavefront is sufficiently stable that it does not enable a real gain with KLIP compared to the classical PSF subtraction, On the contrary, in the case of noisy data, the cross-correlation values vary around a quite small value without

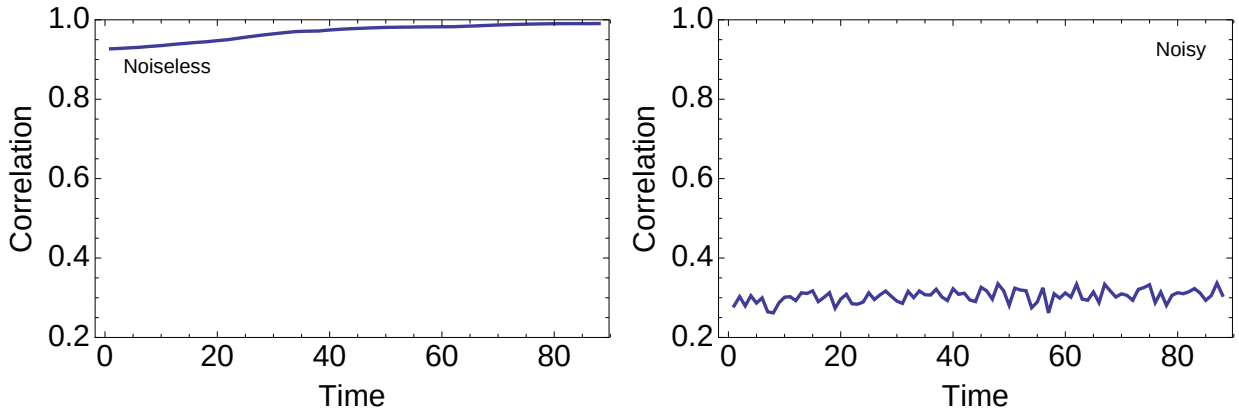

(a) Noiseless (b) Noisy

Figure 9: **HLC OS1 time series - Initial distribution.** Correlation of 47Uma_Slice1 with each slice of betaUma: [left] (a) noiseless data and [right] (b) noisy data.

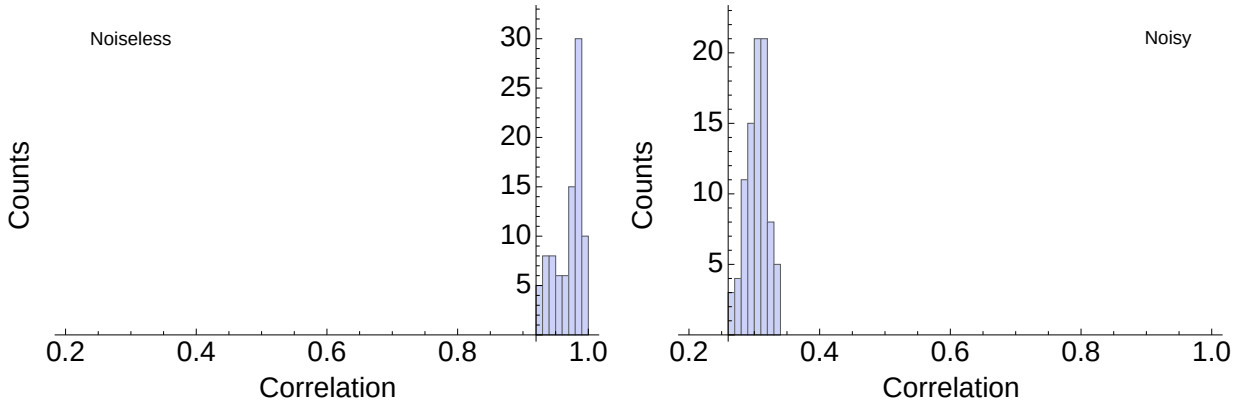

(a) Noisy (b) Noiseless

Figure 10: **HLC OS1 time series - Initial distribution.** Correlation of 47Uma_Slice1 with each slice of betaUma: [left] (a) noiseless data and [right] (b) noisy data.

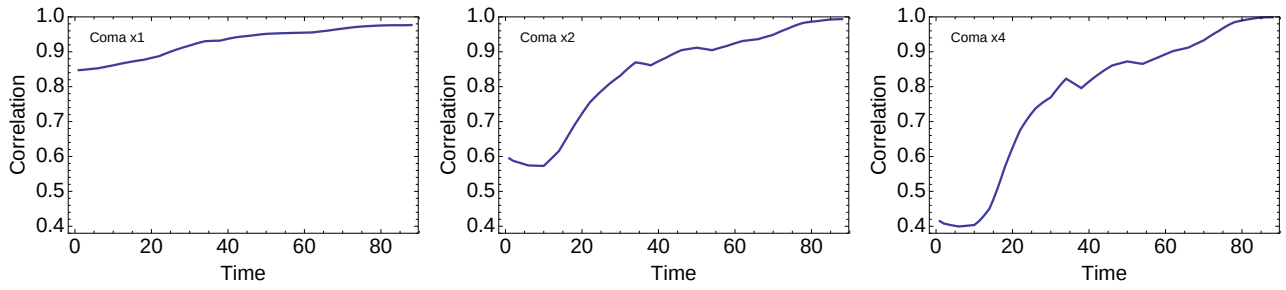

(a) Coma x1 (b) Coma x2 (c) Coma x4

Figure 11: **HLC OS1 time series - Coma distribution.** Correlation of 47Uma_Slice1 with each slice of betaUma for different levels of coma: [left] (a) coma x1 (reference amount), [middle] (b) coma x2 and [right] (c) coma x4. These data are noiseless.

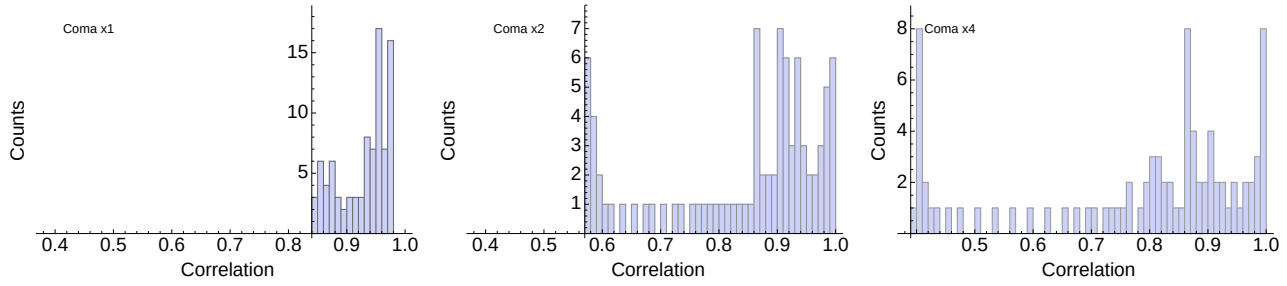

(a) Coma x1 (b) Coma x2 (c) Coma x4

Figure 12: **HLC OS1 time series- Coma distribution.** Correlation of 47Uma_Slice1 with each slice of betaUma for different levels of coma: [left] (a) coma x1 (reference amount), [middle] (b) coma x2 and [right] (c) coma x4.

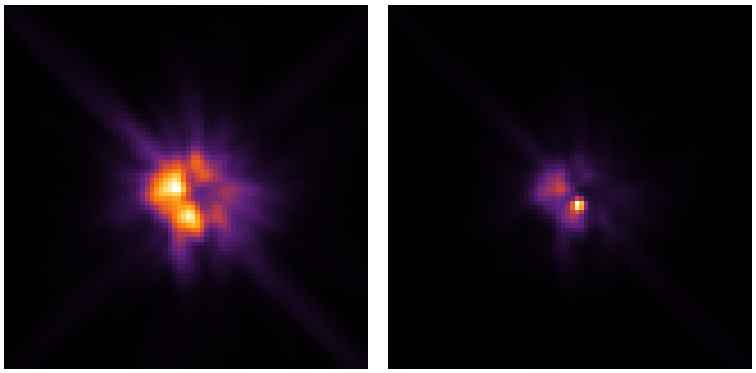

Figure 13: **HST-NICMOS data.** Data used for the correlation computation in the HST-NICMOS case. [Left] First slice of the target cube, [right] first slice of the reference cube.

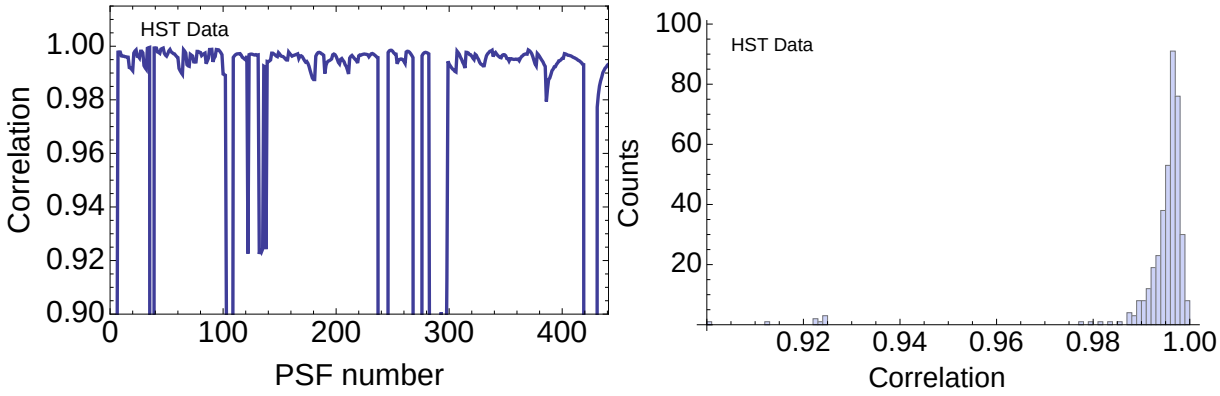

Figure 14: **HST-NICMOS data.** Results of correlation computations. [Left] Evolution of the correlation with time, during reference acquisition, [right] histogram of the correlations during reference acquisition.

increasing with time, indicating that the telescope is stabilized. But there is only enough photons in the image to really capture the first few KLIP modes, the higher order KLIP modes are photon noise limited.

We compare these results to the evolution of cross-correlation with time in the case of HST data (cf. Figure 14). The cross-correlation values vary around a quite high mean without increasing or decreasing with time, indicating that the telescope is stabilized. Only a few values are quite small and indicate very low-correlated data that can be easily eliminated from the reduction process. What differs from the noiseless case of the HLC OS1 data set is that the cross-correlation values follow a Gaussian distribution for the HST data while they follow a more uniform distribution in the case of HLC OS1 data. On the contrary, the cross-correlations values for the noisy HLC OS1 data set is closer to a Gaussian distribution, thus closer to the statistics of the HST data. But the cross-correlation values are quite small. These results give insight into which reduction method should be used, depending on the data statistics. If the cross-correlation values are quite high, one should use the classical PSF subtraction; if not, then one should use KLIP instead.

This is what we can observe for the coma distribution in figures 11 and 12. Increasing the amount of coma increases the decorrelation between the data and the reference. Associated with high values of cross-correlations, this could explain why KLIP performs slightly better than the classical PSF subtraction in the cases with bigger amounts of coma.

Our interpretation is that the KLIP performance with respect to those of the classical PSF subtraction depends on the stability and statistics of the data noise distribution. The thermal model used to simulate the data may be one of the key factors in this process. More recent thermal models (OS2-3-4) might feature updated noise statistics. The preliminary results that we obtained on the OS3 time series simulated with a different model from OS1 (cf. section 4) seems to confirm this interpretation. Moreover, the amount of data provided for the OS3 time series is not sufficient yet to be completely confident about this statement. The confirmation of the interpretation will be part of a future task (cf. section 7), as soon as we receive enough data to perform a good statistical analysis.

3 SCP OS1 TIME SERIES

This section covers our analysis of the broadband SPC OS1 time series simulated with a shaped-pupil coronagraph (SPC). We assess the applicability of the KLIP algorithm and compare its performance with the classical PSF subtraction on temporal data simulated with a SPC coronagraph for the observing scenario OS1. We first describe the simulated data that STScI received from JPL in sub-section 3.1, before reducing and analysing them in section 3.2.

3.1 DESCRIPTION OF SIMULATIONS

A set of images were generated for the WFIRST-AFTA OS1 observing scenario using the shaped pupil coronagraph at 18 wavelengths over the 728 - 872 nm wavelength range. The images represent 250 sec integrations per timestep on Beta UMa and 47 UMa. Model spectra (A0V for Beta UMa, G0V for 47 UMa) were integrated over the sub-bands to weight the image at each wavelength. The image sampling is 0.35 λ/D @ 0.8 μm. The input aberrations are the same as those used in the previous HLC OS1 simulations - tip, tilt, and focus are considered to have been perfectly corrected. These images are noiseless. The coronagraph consisted of a shaped pupil mask in a pupil plane after the deformable mirrors. At the intermediate focal plane a bow-tie-shaped mask was applied; this had inner and outer radii of 2.5 and 9 λ/D @ 0.8 μm and an opening angle of 65 degrees. At a subsequent pupil plane a Lyot stop was applied, which consisted of a circular annular aperture. The dark hole was optimized for X+Y polarizations (the IFS is not polarization filtered, unlike the imaging channel). Images were generated separately for the X and Y polarizations and then combined.

OS1 time series with the shaped pupil coronagraph - John Krist (JPL) - 5 March 2015

Target and reference:
OS1.0_beta_Uma_SPC_XYPOL_IFS_sequence_noiseless.fits
OS1.0_47_Uma_SPC_XYPOL_IFS_sequence_noiseless.fits
Other files:
3-D array (63,63,22) with the star offset by 22 different X,Y offsets from the center of the field (the offsets are in field_offsets.fits). Offsets are only in one-quarter of the field (flip and rotate as needed for the PSF in another quadrant). These are monochromatic PSFs @ 0.8 μm:
field_psfs.fits
2-D array (2,22) containing the X (1st column) and Y (2nd column) offsets of the star in the corresponding field_psf.fits array. The offsets are in lambda/D units @ 0.8 μm.
field_offsets.fits
2-D array (63,63) containing the focal plane mask sampled at the resolution of the final image (0.35 lambda/D @ 0.8 μm*).* focal_plane_mask.fits

3.2 PRELIMINARY RESULTS USING ONLY ONE WAVELENGTH OF THE DATA SET

Before reducing the data with KLIP, we collapse the science data cubes (47 Uma) for each wavelength to obtain 18 long exposure raw images (one per wavelength). One KLIP library per wavelength is then built using the reference PSF data cubes for beta Uma. Each KLIP library is decomposed in principal components through the KLIP algorithm. This reduction process is the same as in figure 1, except that the polarizations X and Y have already been collapsed and that we do the same at each wavelenght.

Figure 15 shows the results of the reductions for the 9th wavelength on 18 (central wavelength). We represent on the same dynamic range the long exposure raw science data cube (all

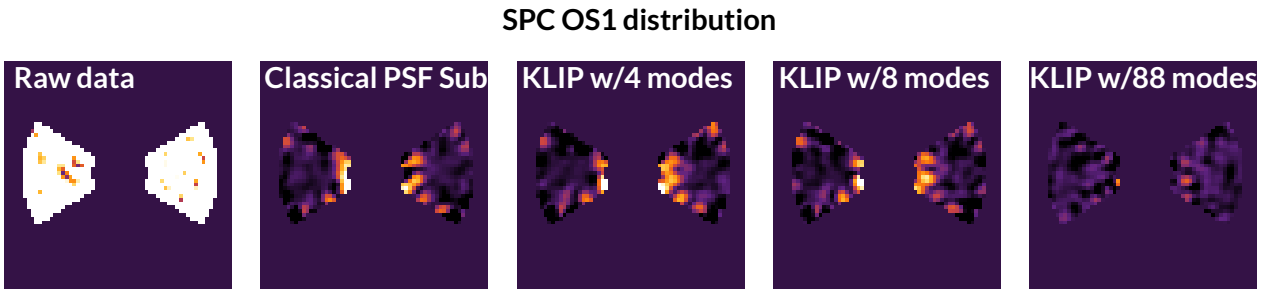

Figure 15: **SPC OS1 time series**. Comparison of the raw data and three different reductions for the 9th wavelength. From left to right with same dynamic range: raw image (long exposure), image processed with classical PSF subtraction, image processed with KLIP 4 modes, image processed with KLIP 8 modes and image processed with KLIP 88 modes. The two techniques show a relatively good PSF subtraction compared to the raw image. Two planet candidates are detected on both sides of the central occultation for both the reductions with classical PSF subtraction and KLIP with 4 modes.

slices collapsed), the classical PSF subtraction reduction and the KLIP reduction with 4, 8 and 88 modes. The two techniques show a relatively good PSF subtraction compared to the raw image but the identification of planet candidates is quite difficult in the light of the shape of the unocculted PSF. Figure 16 illustrates the shape of the PSF for two different offsets: on the middle, the offset is through the x-axis only and we can recognize the characteristic shape of the shaped-pupil coronagraph PSF with one central lobe and two side lobes; on the right, the offset is through both the x and y axis, and one of the lobes is hidden by the bow-tie focal plane mask, which is represented on the left of figure 16.

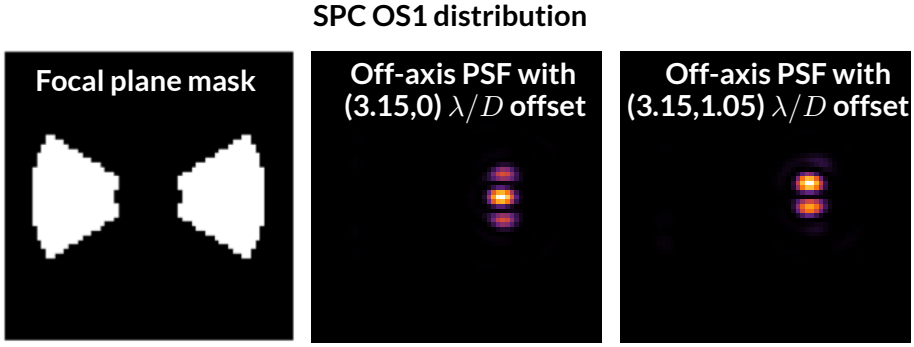

Figure 16: **SPC OS1 time series**. [Left] Bow-tie mask: Focal plane mask sampled at the resolution of the final image, [middle] unocculted PSF with an offset 3.15 λ/D with its three visible lobes and [right] unocculted PSF with offsets of 3.15 λ/D and 1.05 λ/D@ 0.8 μm with only two lobes visible,the third being hidden by the bow-tie mask.

We also report the KLIP throughput as a function of the number of KLIP modes for a planet at $3.15\lambda/D$ from the star (Figure 17) and the gain in contrast with respect to the long exposure raw data as function of the separation (Figure 18). These curves take into account the KLIP throughput. KLIP enables a similar gain in contrast as classical PSF subtraction. Increasing the number of KLIP modes improves slightly the gain at small separations. The gains compared to the raw data are quite significant, going from a gain of about 10 for a few KLIP modes used at

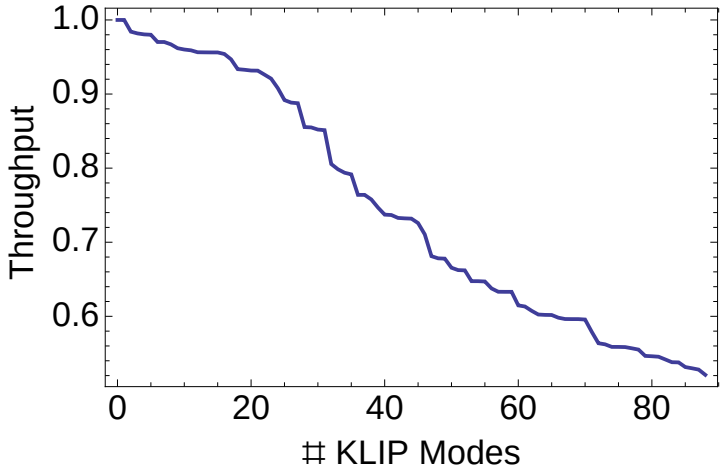

Figure 17: **SPC time series.** KLIP throughput as a function of the number of KLIP modes for a planet at $3.15\lambda/D$ from the star.

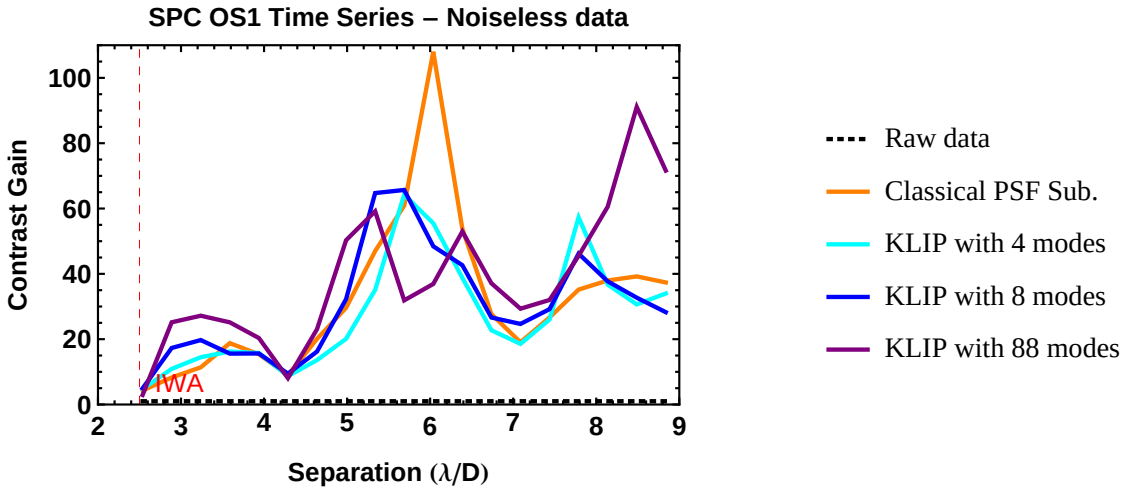

Figure 18: **SPC time series.** Contrast gain as a function of separation. These curves take into account the throughput of KLIP. KLIP enables a similar or better gain in contrast than classical PSF subtraction for all separations. Increasing the number of KLIP modes improves the gain.

small separations to a gain of 60 for the reduction with 88 KLIP modes at higher separations.

4 HBLC OS3 TIME SERIES

This section covers our analysis of the simulated broadband HBLC OS3 time series. We assess the applicability of the KLIP algorithm and compare its performance with the classical PSF subtraction on temporal data simulated with an HLC coronagraph for the observing scenario OS3. We first describe the simulated data that STScI received from JPL in the sub-section 4.1, before reducing and analyzing them in the section 4.2.

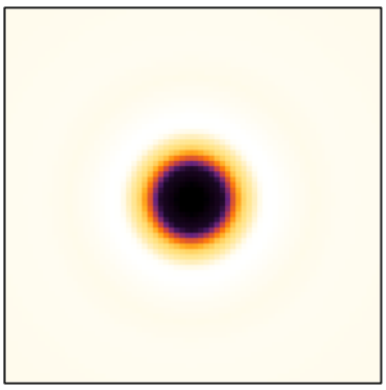

Figure 19: **HBLC OS3 time series**. Map of the PSF peak at each location in the field.

4.1 DESCRIPTION OF SIMULATIONS

These simulations model the OS3 scenario (like OS1 but with a different telescope & coronagraph structural configuration). Two sets are provided, with and without control of low order aberrations (Z5-Z11) using the deformable mirror (LOWFC). There are 8 beta UMa images and 17 each for 47 UMa and 61 UMa. For 47 UMa, images are provided with and without planets added. The image sampling is 0.35 λ/D per pixel. No noise was added on the data.

OS3 @ L2 (Earth excluded) time series - John Krist (JPL) - 18 April 2015

Data without DM LOWFC

OS3.0_beta_Uma_HLC_polX_no_earth_sequence_noiseless.fits

OS3.0_47_Uma_HLC_polX_no_earth_sequence_noiseless.fits

OS3.0_47_Uma_HLC_polX_no_earth_sequence_noiseless_no_planets.fits

OS3.0_61_Uma_HLC_polX_no_earth_sequence_noiseless.fits

Data with DM LOWFC

OS3.0_lowfc_beta_Uma_HLC_polX_no_earth_sequence_noiseless.fits

OS3.0_lowfc_47_Uma_HLC_polX_no_earth_sequence_noiseless.fits

OS3.0_lowfc_47_Uma_HLC_polX_no_earth_sequence_noiseless_no_planets.fits

OS3.0_lowfc_61_Uma_HLC_polX_no_earth_sequence_noiseless.fits

Other files

peak_map.fits = map of the PSF peak at each location in the field

unocculted_psf.fits = unocculted image of the star

4.2 PRELIMINARY RESULTS USING BETA UMA AS A REFERENCE INSTEAD OF 61 UMA

Before reducing the data with KLIP, we perform exactly the same preparatory processing of the data as for the intial distribution (cf. section 1.2 and Figure 1), except that we have only the X polarization. In these preliminary results, we have not used 61 Uma as the reference but beta Uma instead. The former will be part of the future tasks (cf. in section 7).

In the figure 20, we represent the raw and post-processed images for the cases without and

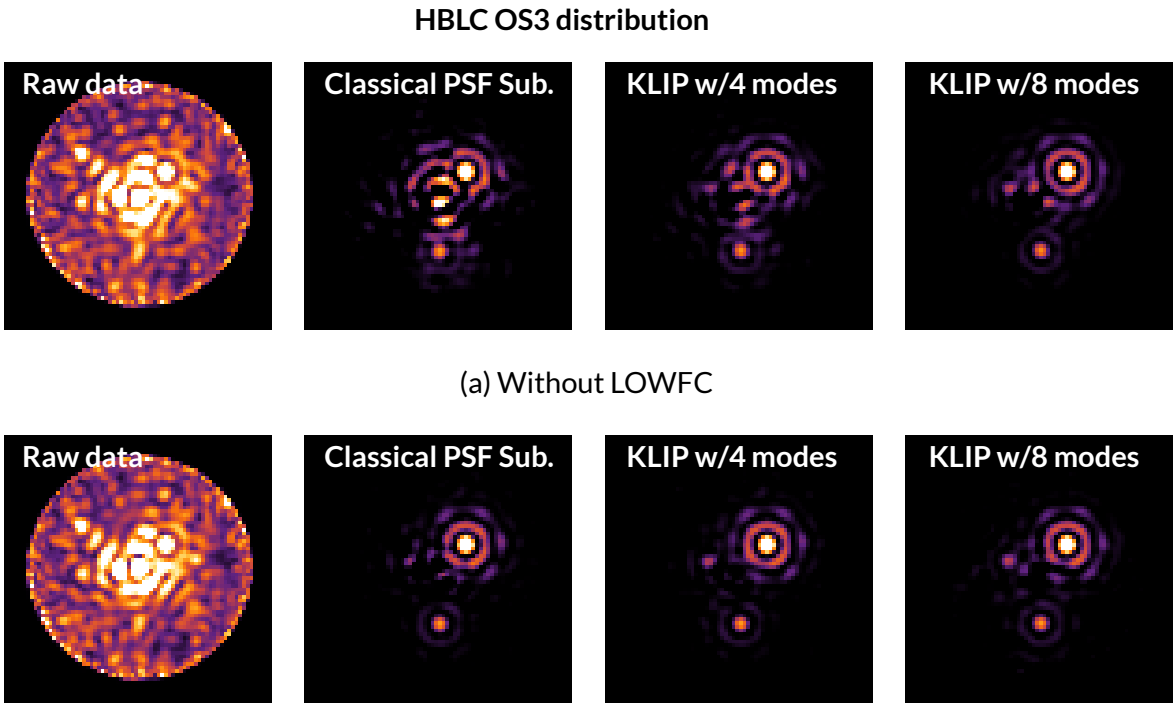

(a) Without LOWFC

(b) With LOWFC

Figure 20: **HBLC OS3 time series**. Comparison of the raw data and three different reductions. Top: (a) noiseless data without LOWFC. Bottom: (b) noiseless data with LOWFC. From left to right with same dynamic range: Raw image (long exposure), Image processed with Classical PSF subtraction, image processed with KLIP 4 modes and image processed with KLIP 8 modes. The two techniques show a relatively good PSF subtraction compared to the raw images for both the cases wihtout and with LOWFC. The reduction quality is improved by the KLIP reduction compared to the classical PSF subtraction; the more KLIP modes used, the better the result.

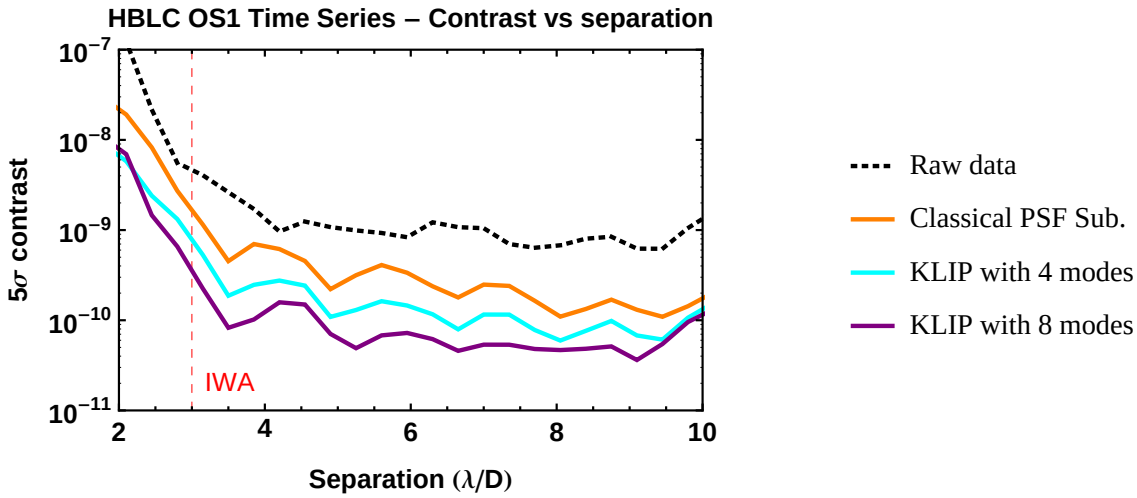

Figure 21: **HBLC OS3 time series**. 5-sigma contrast curves as a function of separation without LOWFC. These curves take into account the KLIP throughput. KLIP enables a better contrast than classical PSF subtraction for all separations. Increasing the number of KLIP modes improves the contrast. We emphasize that levels of contrast such as 10^{-10} might not be achieved in practice by WFIRST-AFTA because of other limiting factors not included in the simulations presented here.

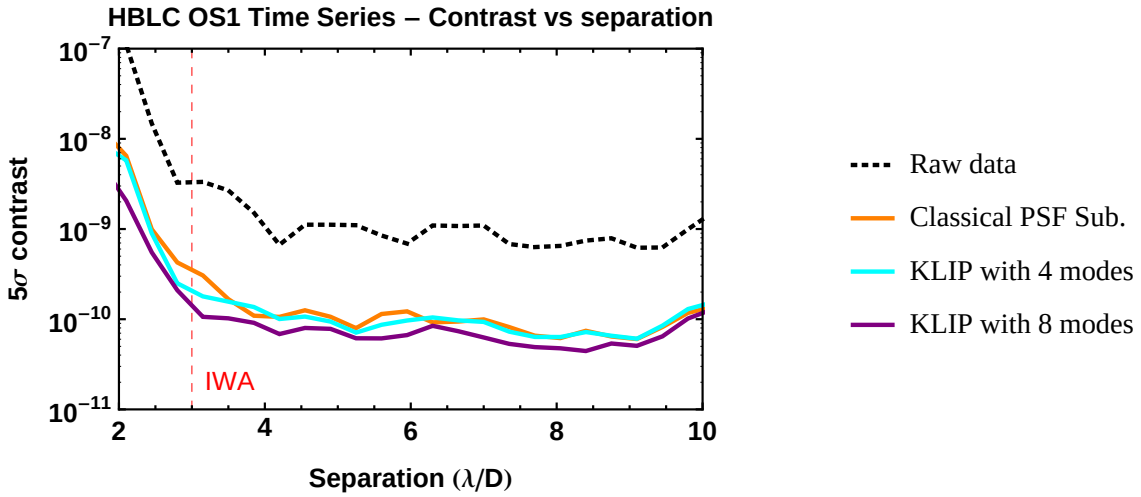

Figure 22: **HBLC OS3 time series.** 5-sigma contrast curves as a function of separation with LOWFC. These curves take into account the KLIP throughput. The performance is similar for the three reductions with a slightly improvement at small separation for the KLIP reduction. Here again, increasing the number of KLIP modes improves the contrast but to a lesser extent. We emphasize that levels of contrast such as 10^{-10} might not be achieved in practice by WFIRST-AFTA because of other limiting factors not included in the simulations presented here.

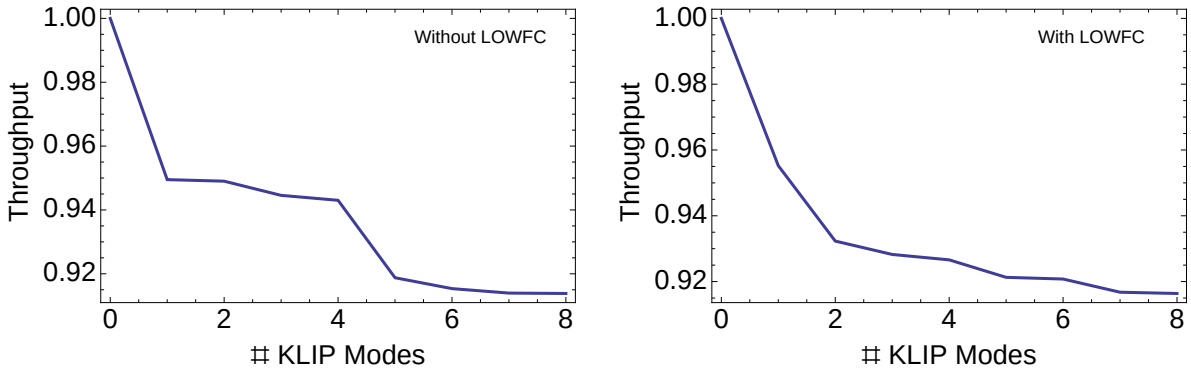

Figure 23: **HBLC OS3 time series.** KLIP throughput as a function of the number of KLIP modes for a planet at $3.15\lambda/D$ from the star. [Left] without LOWFC [right] with LOWFC.

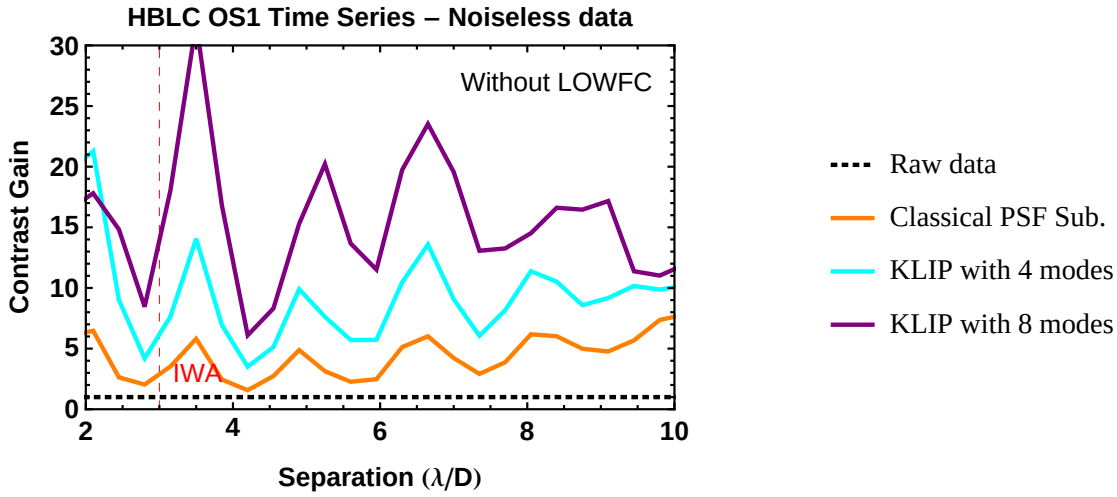

Figure 24: **HBLC OS3 time series**. Contrast gains as a function of separation for the case without LOWFC. These curves take into account the KLIP throughput. The classical PSF subtraction enables a contrast gain of 5 at the most for small separations. The contrast gain is better than 5 for the two reductions with KLIP. The 8 modes reduction enables a maximum gain of 30 for a separation of $3.5\lambda/D$.

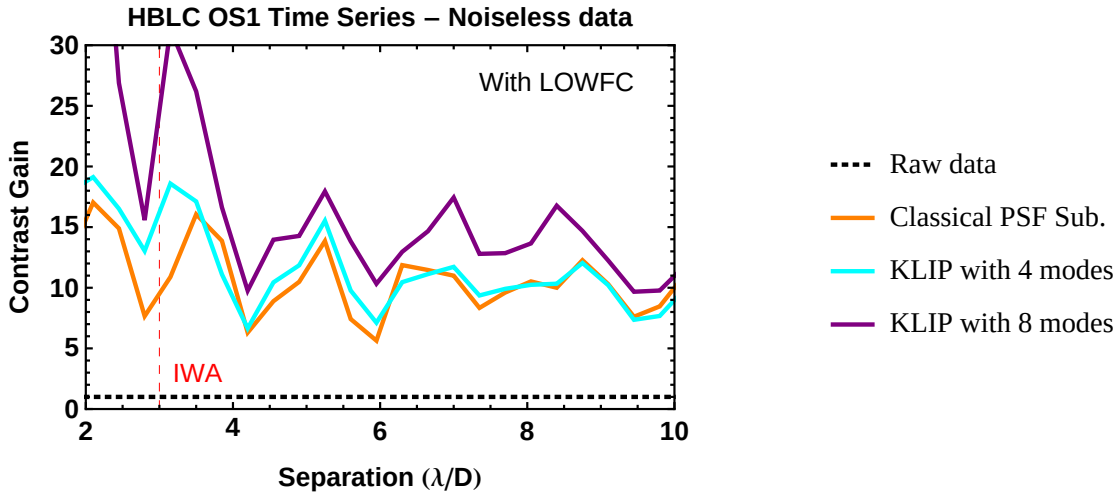

Figure 25: **HBLC OS3 time series**. Contrast gains as a function of separation for the case with LOWFC. These curves take into account the KLIP throughput. All the reductions enable a minimum contrast gain of 5. The 8-mode KLIP reduction enables a gain up to 30 for a separation of $3\lambda/D$, compared to the raw data.

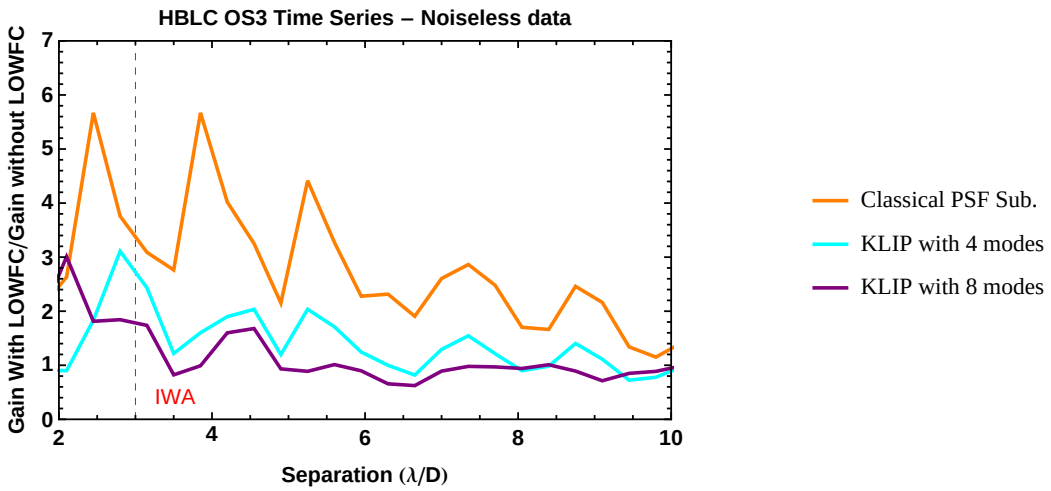

Figure 26: **HBLC OS3 time series**. Post-processing performance gain ratio (with LOWFC compared to without LOWFC). The gains are better with the LOWFC than without for all the reductions. This is the classical PSF subtraction reduction that benefits the more from the presence of LOWFS. The KLIP reductions benefit also from the presence of the LOWFC but to a lesser extent.

with LOWFC. Without LOWFC, KLIP performs much better than the classical PSF subtraction. The three planets are very well detected with KLIP w/8 modes, whereas only two are barely visible with the classical PSF subtraction. Even the case KLIP w/4 modes allows a better detection, if not ideal, than the classical PSF subtraction for the third planet. The LOWFC provides enough stability to improve the performance of PSF subtraction in all cases. But we clearly have a better detection with KLIP than with classical PSF subtraction at small separations. The ultimate performance is currently limited by the small size of the reference PSF library (8 PSFs for beta Uma).

These observations are confirmed by the 5-sigma contrast curves for the cases without and with LOWFC, shown in figures 21 and 22 respectively. To compute the contrast curves we have used the data set without planets. To convert to contrast, we divided each image in the raw data cube by the TOTFLUX value specified in the FITS header. We divided each processed image by the peak_map.fits file, representing the map of the PSF peak at each location in the field (cf. Figure 19). These contrast curves do take into account the throughput of KLIP. Contrary to the observations we made for the OS1 time series, we report a clear improvement with KLIP even with a small number of modes. We emphasize that the levels of contrast represented in figures 21 and 22 might not be achieved in practice by WFIRST-AFTA because of other limiting factors not included in the simulations presented here.

We represent in figure 23 the KLIP throughput as a function of the number of modes for a planet at $3.15\lambda/D$. Because of the small number of KLIP modes, the throughput is quite high, enabling good contrast levels.

Finally, if we look at the contrast gains as a function of separation for the cases without (Figure 24) and with LOWFC (Figure 25), we can quantify the performance of the reductions. Except for the reduction with the classical PSF subtraction in the case without LOWFC, we report

a gain above 5. For both the cases without and with LOWFC, the best performing reduction is KLIP with 8 modes, which enables a contrast gain up to 30 at small separations. KLIP with 4 modes performs better than the classical PSF subtraction without LOWFC and only slightly better than the classical PSF subtraction in presence of LOWFC.

If we compute the ratio of contrast gains with and without LOWFC as function of separation (Figure 26), we can determine the impact of the LOWFC system on the post-processing performance. The gains are more important in the presence of LOWFC, for all reduction techniques taken together. The technique that benefits most from the LOWFC is the classical PSF subtraction. The LOWFC enables a gain multiplication by a factor of 3 for this technique at $3\lambda/D$. Some gain multiplications by factors of 2.8 and 1.8 are observed respectively for KLIP with 4 modes and KLIP with 8 modes at $3\lambda/D$.

II SPECTRAL DIVERSITY

This part focuses on our effort to exploit the spectral diversity offered by multi-spectral images to detect exoplanets. We assess the applicability of the spectral deconvolution technique to simulated multi-spectral images generated at STScI, with one deformable mirror and a coronagraph.

5 WFIRST-AFTA-LIKE SIMULATED DATA AND SPECTRAL DECONVOLUTION

5.1 CLASSICAL SPECTRAL DECONVOLUTION

Introduced by Sparks and Ford [21] the Spectral Deconvolution method, as we will refer to in the following as the "Classical Spectral Deconvolution" (CSD), takes advantage of the chromatic behavior of the coronagraphic PSF to disentangle the signal of a planet from the speckles. A classical result is that both the position and the size of the speckles is proportional to the wavelength λ. With a λ-factor rescaling, it is possible to make the speckles static as a function of wavelength. Figure 27 illustrates this by showing both the spatial and spectral evolutions of the speckle field (without deformable mirror) before and after rescaling by a factor of λ. The intensity of one spaxel, which describes all the pixels of the data cube situated at the same spatial position, is then spectrally modulated in the non-rescaled data-cube, whereas it evolves as a function of a low-order polynomial such as $P_n(\lambda) = \sum_{n=0}^{+\infty} \frac{a_n}{\lambda^n}$ in the rescaled data-cube. Figure 28 shows the spectral evolutions of a pixel intensity as a function of wavelength before and after rescaling. Thus, we can subtract the speckles from the data-cube by fitting each spaxel by a low-order polynomial $P_n(\lambda)$, typically with $k = 4$ [21]. The data to be processed must fulfill three conditions if we want the CSD method to be successful:

- The speckle pattern spatially must scale as a function of λ.
- The spectral evolution of a spaxel intensity can be modeled, after rescaling, by a low-order polynomial such as $P_n(\lambda) = \sum_{n=0}^{+\infty} \frac{a_n}{\lambda^n}$ leading to a relatively good subtraction of the speckles.
- The planet intensity evolution can be modeled, after rescaling, by a high-order polynomial in $1/\lambda^n$ with n positive, provided that the spectral bandwidth is sufficiently large.

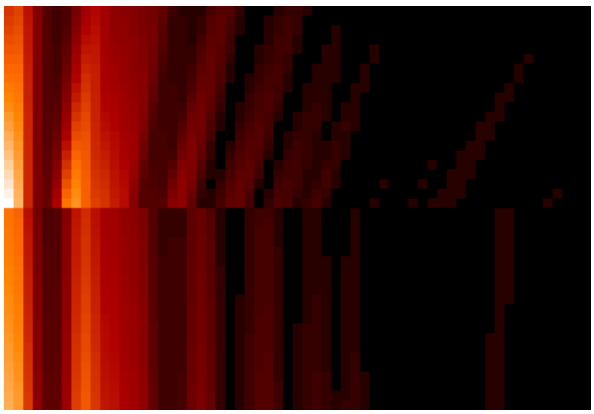

Figure 27: Spatial and spectral evolutions of pixel intensity with the wavelength [top] before and [bottom] after rescaling by a factor of λ, without DM. Only the right part of the data-cube is represented here. The horizontal axis represents the separation and the vertical axis represents the wavelength.

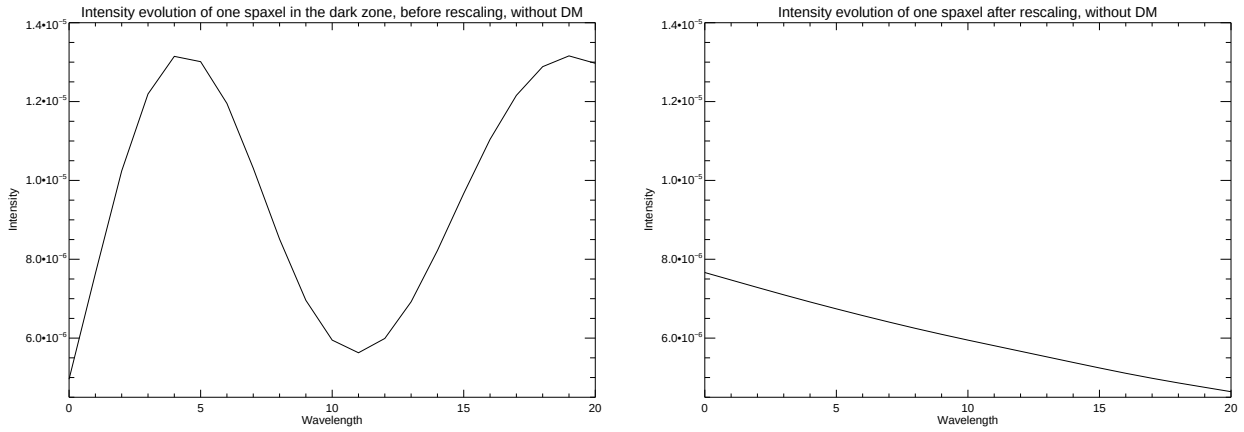

(a) Before rescaling

(b) After rescaling

Figure 28: Spectral evolution of pixel intensity with the wavelength (a) before and (b) after rescaling by a factor of λ, without DM.

The "bifurcation radius" [22] represents the limit separation under which the last condition is not fulfilled. It can be written as:

$$BR = 2.44 \times \frac{\lambda_{\text{min}}}{D} \frac{\lambda_0}{\Delta\lambda}, \tag{2}$$

where $2.44 \times \frac{\lambda_{\text{min}}}{D}$ is the object extent at the minimum wavelength and $\frac{\Delta\lambda}{\lambda_0}$ the spectral bandpass. The bifurcation radius is inversely proportional to the bandpass. The larger the bandpass, the smaller the bifurcation radius.

Consequently, the success of the method resides in a good compromise between the best subtraction of the speckles and the least loss of the planet signal. The choice of the polynomial order is crucial, as well as regularization-like strategies such as iterative techniques [22, 26] or companion masking [27].

5.2 SIMULATION TESTS

We simulated several cubes of "WFIRST-AFTA-like" images of dimensions 128 x 128 x 21, where 128 is a number of pixels and 21 is the number of different wavelengths. Unless otherwise specified, we assume that the bandpass is $\Delta\lambda/\lambda_0 = 20\%$. The aperture is circular and without any obscuration or spiders. We consider 7 nm of amplitude and phase errors. We emphasize that this amount of aberrations is quite law and whereas this is sufficient for our study, this leads to unrealistic levels of contrast that might not be achieved in practice by WFIRST-AFTA. A perfect simulated coronagraph provides the starlight suppression. By "perfect", we mean that the correction is total and fully achromatic for a plane wave. There is no source of noise in these preliminary images, other than residual speckles. Figure 29 shows some examples of simulated images. In the following, we will use different data-cubes without any planet:

- A first set of data-cubes does not contain any correction by a deformable mirror (DM) (Sub-figure 29(a));
- A second set of data-cubes simulates a 32x32 DM that performs a phase correction in the pupil plane at $\lambda_0 = \lambda_{\text{min}} + \delta\lambda/2$, leading to a dark zone over 3-10 lambda/D (Sub-figure 29(b)). We use a mask to select only the dark zone (Sub-figure 29(c)). Sub-figure 29(d) shows the dark zone of the image simulated with one DM;
- A third set of data-cubes simulate some planets situated in the dark zone for different bandwidths, without any speckles. The planets are simulated using a non-coronagraphic point-spread function (PSF). We assumed a white spectrum for this study.

In the following, we perform two sets of tests. The first set focuses on the simulated data cube without DM in order to illustrate how CSD works. The second set of tests focuses on simulated data cubes with one DM to understand how CSD performs in the particular case of WFIRST-AFTA-like images. For each set of tests, we consider three different data cubes:

- One cube with only speckles
- One cube with only the planet
- One cube with both speckles and planets (the sum of of the two previous cubes)

We also define the final gain as the gain on the speckle subtraction divided by the loss of planet flux.

Tests without DM. We consider here two different bandpasses: 36% and 20%. The contrast between the simulated planet and the star is 5.10^{-6}. The planet separation is about $10\lambda_0/D$. For each of the cubes simulated without DM, we perform a PSF subtraction by fitting each spaxel with a 4th-order polynomial:

$$P_4(\lambda) = a_0 + a_1\frac{1}{\lambda} + a_2\frac{1}{\lambda^2} + a_3\frac{1}{\lambda^3} + a_4\frac{1}{\lambda^4} \quad (3)$$

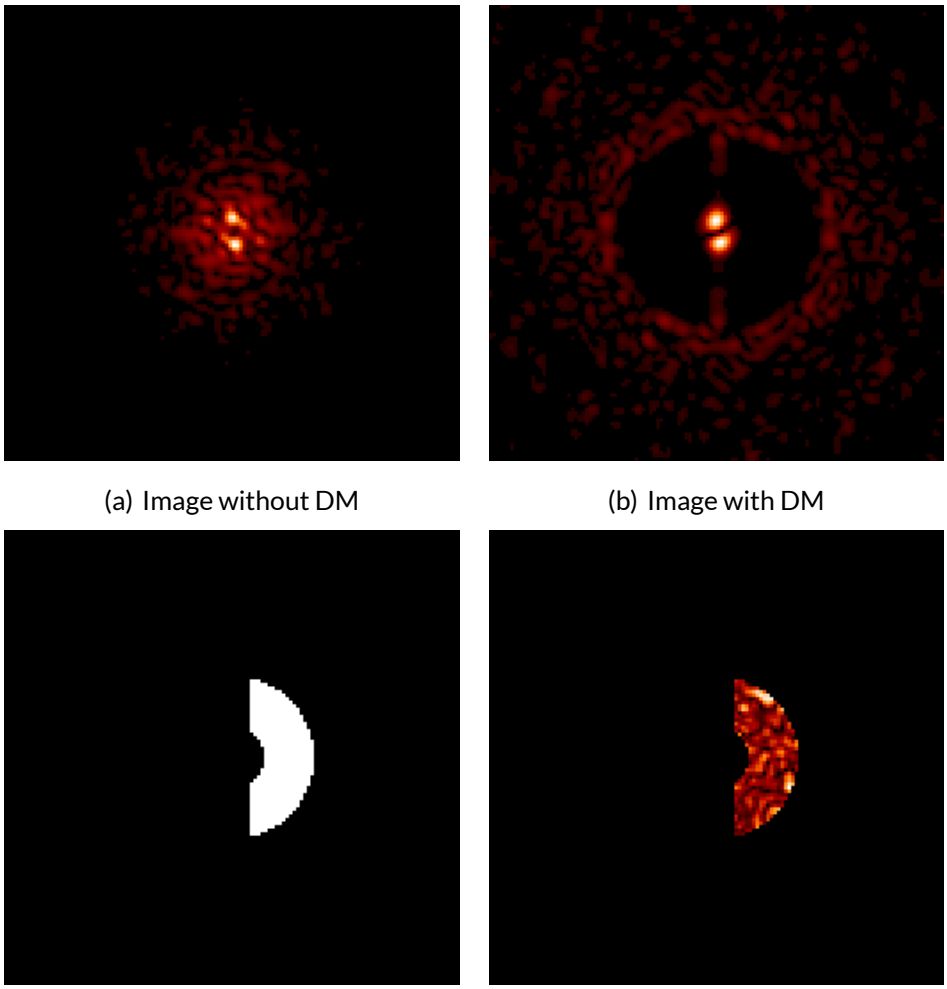

(a) Image without DM (b) Image with DM

(c) Mask (d) Image with DM and with Mask

Figure 29: Examples of simulated images

We then collapse the data cube in a single broadband image. We represent the collapsed data cubes with both speckles and the planet in Figure 30. The sub-figure 30(a) is the result for a 36% bandpasses: the planet is detected. The sub-figure 30(b) is the result for a 20% bandpass: there is no clue of the planet in this image because we are under the detection limit. If we compute the value of the bifurcation radius (cf. Eq. 2) for 36% and 20% bandpass, we obtain $6.7\frac{\lambda_{\text{min}}}{D}$ and $12.2\frac{\lambda_{\text{min}}}{D}$ respectively. This means that a planet at $10\frac{\lambda_{\text{min}}}{D}$ is theoretically detected in the 36% bandpass data cube, but it is not in the 20% one.

We can understand these results by analyzing the contrast curves of the data cube with the speckles only and the flux of the data cube with the planet only (cf. Figure 31.) We compute the contrast curves which are defined by the 5σ level of residual speckles normalized to the non-coronagraphic central star. These curves are computed before and after CSD. To compute these curves, we use the post-processed data cube with the speckles. We also represent the flux of the planet before and after CSD, using the post-processed data cube with the planet. The 5σ level of residual speckles is about 3.10^{-5} (dotted lines) and $\simeq 5.6.10^{-8}$ (black solid line), before and after CSD, respectively. Thus, the gain from the speckle subtraction is of the order

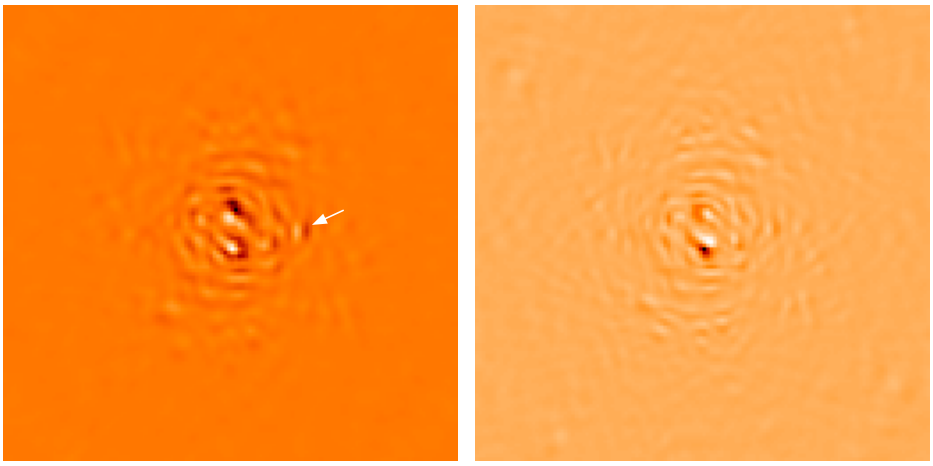

(a) 36% bandpass, without DM (b) 20% bandpass, without DM

Figure 30: Single broadband image after CSD. These images are computed by collapsing the cubes of monochromatic images after CSD and after rescaling for (a) 36% and (b) 20% bandpasses. The arrow indicates the position of the planet.

of 500. AT the same time, the planet flux is divided by about 100 and 20 for 20% and 36% bandpasses respectively. This means that a part of the planet flux is also subtracted. Even if the gain on the speckle subtraction is higher than the loss on the planet flux, it may not be sufficient to detect the planet. For example, in the 20% bandpass case, the residual contrast between the planet and the star residuals before CSD is > 10. And the final gain is about 6 only. We are then under the detection limit here, which is consistent with the definition of the bifurcation radius (cf. Eq. 2). This is not the case for the 36% bandpass data cubes. The final gain is around 30, which is higher than the residual contrast between the planet and the star residuals before CSD. The planet is detected.

Tests with DM. We saw in the previous paragraph that the planet at a separation of about $10\lambda_0/D$ is not detected after post-processing with CSD for a 20% bandpass. We will not try to detect a similar planet in data cubes simulated with DM with this bandpass. We instead assume that we have a 36% bandpass. The value of the bifurcation radius is then $6.7\frac{\lambda_{\text{min}}}{D}$. The planet separation is still about $10\lambda_0/D$. The contrast between the simulated planet and the star is now set to 1.10^{-9}. We still perform a PSF subtraction by fitting each spaxel with the 4th-order polynomial of equation 6. The collapsed data cubes with both speckles and the planet are represented in the sub-figure 32(b).

As before, we compute the contrast curves before and after CSD (cf. Figure 33). The 5σ level of residual speckles is still about 3.10^{-5} for the simulated images without DM (dotted lines). In the data cubes simulated with a DM, the contrast curves vary from about 8.10^{-10} to 5.10^{-9} depending on the wavelength (dashed lines). After CSD, the level of contrast drops to about 1.10^{-10} (black solid line). The gain of contrast is less than 10. At the same time, the planet flux drops from about 1.10^{-9} (asterisks) to 5.10^{-11} (black diamond). The loss of flux is about 20.

Hence, the planet is more subtracted than the speckles. The final gain is under 1. The planet is not detected. Actually, in this case, the post-processing with CSD makes things worse because with a contrast of 1.10^{-9}, it is possible to distinguish the planet without any post-processing on a single monochromatic image at the central wavelength (cf. Sub-figure 32(a)).

5.3 CHROMATIC BEHAVIOR OF SPECKLES IN HIGH-CONTRAST IMAGES

If CSD fails to enhance the final gain, it is clearly because of the chromatic behavior of the speckles. Indeed, this behaviour is not the same in the images simulated with a DM as in the images simulated without DM. Figure 42 shows both the spatial and spectral evolutions of the speckle field with DM and without planet before and after rescaling. We can recognize the dark hole on the sub-figure 34(a). In the sub-figure 34(b), we use the mask defined in the figure 29(c) to hide the zones not corrected by the DM in order to properly see with a good dynamic range the speckle evolution in the dark zone. Whereas the speckles that are not in the dark zone are properly rescaled, this is not the case for the speckles in the dark zone that continue to move spatially with the wavelength. The consequence of this is that the spectral evolution of a pixel cannot be modeled anymore, after rescaling, by a low-order polynomial in $1/\lambda^n$ with n positive. The evolution is far more complex than before. Figure 35 shows the spectral evolutions of a pixel intensity as a function of wavelength before and after rescaling.

The chromatic behavior of the speckles in the rescaled data cube could easily be explained with an analytical expression of the speckle field evolution with the wavelength. We do not have currently such a complete expression, but Pueyo et al. [28] showed that the energy of a complex field in the pupil after correction by a DM is proportional to:

$$I\left(\lambda\right) \propto \left| \sum_{k=-\infty}^{+\infty} i^k \frac{\lambda_0^k}{\lambda^k} \right|^2 \tag{4}$$

It is interesting to notice that terms in λ^n with n positive appear. These terms result from phase-induced amplitude errors generated by propagation effects. It is exactly what we see in the sub-figure 35(b). It is clear that the evolution of a pixel intensity with the wavelength can be modeled by a polynomial with terms of the form λ^n with n positive, and not only with terms of the form $1/\lambda^n$ with n positive.

By changing a little bit the model of polynomials used for the fit,

$$P_n\left(\lambda\right) = \sum_{n}^{+\infty} \left[a_n \lambda^n + b_i \frac{1}{\lambda^n} \right], \tag{5}$$

it is possible to better subtract the speckles. We choose for example $n = 10$. The subtracted polynomials are of the following form:

$$\begin{aligned} P_{10}\left(\lambda\right) = {} & a_0 + a_1\lambda + a_2\lambda^2 + a_3\lambda^3 + a_4\lambda^4 + a_5\lambda^5 + a_6\lambda^6 + a_7\lambda^7 + a_8\lambda^8 + a_9\lambda^9 + a_{10}\lambda^{10} \\ & + b_0 + b_1\frac{1}{\lambda} + b_2\frac{1}{\lambda^2} + b_3\frac{1}{\lambda^3} + b_4\frac{1}{\lambda^4} + b_5\frac{1}{\lambda^5} + b_6\frac{1}{\lambda^6} + b_7\frac{1}{\lambda^7} + b_8\frac{1}{\lambda^8} + b_9\frac{1}{\lambda^9} + b_{10}\frac{1}{\lambda^{10}} \end{aligned} \tag{6}$$

Figure 36 shows the contrast curves of the speckle residuals without DM, with DM and after SD. The sub-figure 36(a) shows the results for this adapted SD (ASD), i.e. with polynomials of positive and negative degrees with n = 10. The sub-figure 36(b) shows the results for the classic SD (CSD), i.e. with polynomials of negative degrees only with n = 10 (i.e., with all the coefficients a_n equal to zero). The CSD yields with a gain of about 5, reaching a contrast of about 2.10^{-10}. The speckle subtraction is much better with the ASD, reaching a contrast of about 5.10^{-13}, of the order of the numeric noise level.

5.4 CONCLUSIONS

Even though the CSD method has been successful for post-processing of multi-spectral images, a preliminary study performed on WFIRST-AFTA-like simulated images has showed that it is not possible to use CSD anymore in the context of this space-based mission. Indeed, two conditions for success listed in the sub-section 5.1 are not fulfilled:

- Because of the presence of a DM in the simulated images, the spectral evolution of a pixel cannot be modeled after geometrical rescaling by a low-order polynomial in $1/\lambda^n$ with n positive (cf. Figure 43);
- Fitting the speckles down to the numerical noise is possible using a higher-polynomial with both terms in λ^n and in $1/\lambda^n$. However in this case the limited bandpass of 20% combined with the high-order polynomial leads to a very low planet throughput and the CSD is not usable.

This is exactly the problem that was initially encountered with ground-based high-contrast imaging, albeit now much more severe in the context of AFTA. Indeed, the first post-processing algorithms were able to detect planets but were plagued by low planet throughput and biases that made spectral extraction unreliable if not impossible. Successive attempts included least-square methods and masking (e.g. LOCI, SOSIE), introducing a matrix regularization term reflecting the planet throughput (e.g. Damped-LOCI), and principal component analysis (e.g. KLIP, S4). In this case also for AFTA, regularization strategies have to be considered. Because of the severity of the problem at hand, methods only based on empirical considerations are unlikely to success and we are thus planning to explore combinations of speckle modeling using priors on the wavefront error and empirical regularization.

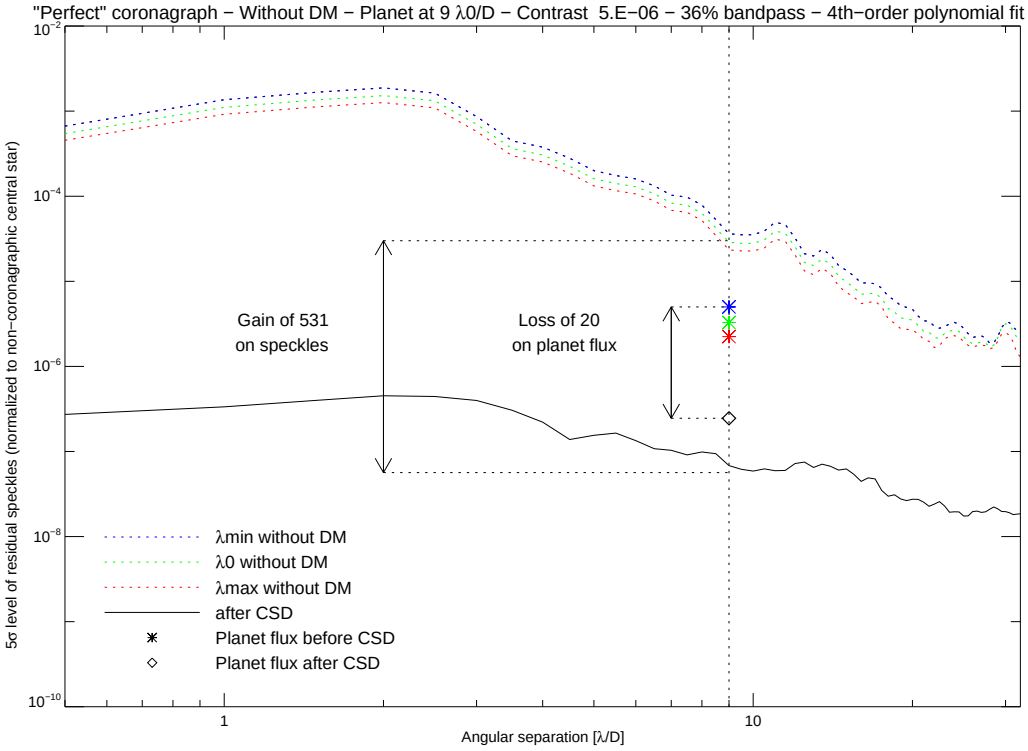

(a) 36% bandpass

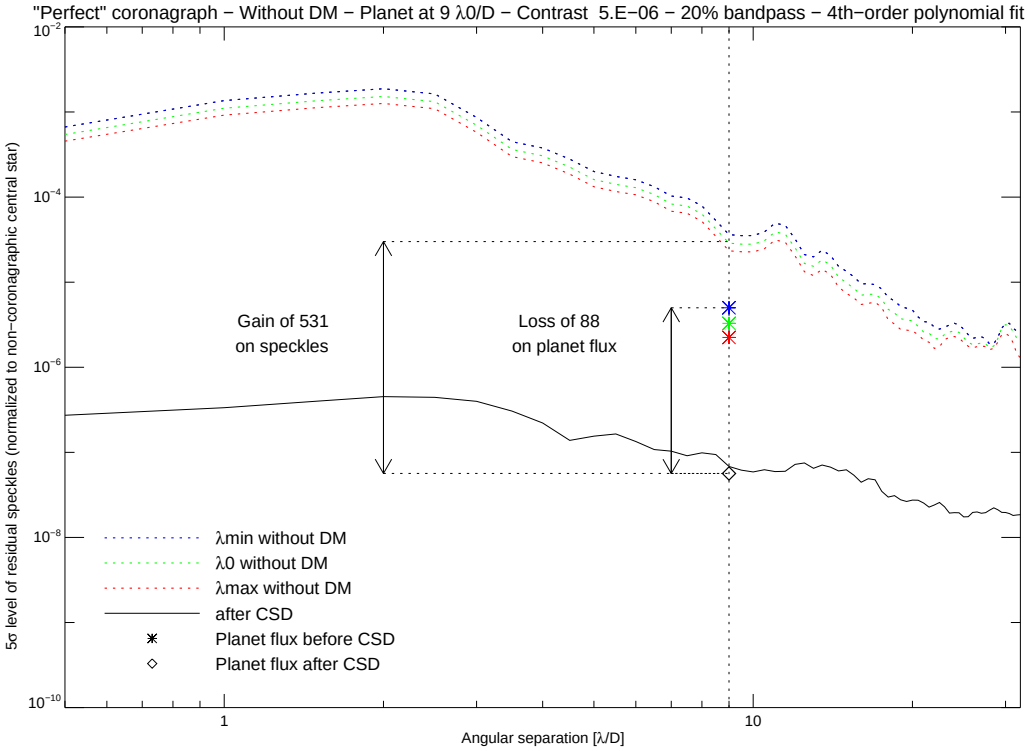

(b) 20% bandpass

Figure 31: 5σ levels of residual speckles normalized to the non-coronagraphic central star for (a) the 36% bandpass and (b) the 20% bandpass. The dotted lines represent the contrast curves before CSD of the data cube of speckles for the minimum (blue), central (green) and maximum (red) wavelengths. The black solid line represents the contrast curves after CSD of the single broadband image. Asterisk-shaped points represent the flux of the planet before CSD for the minimum (blue), central (green) and maximum (red) wavelengths. The diamond-shaped point represents the flux of the planet after CSD of the single broadband image with the planet only.

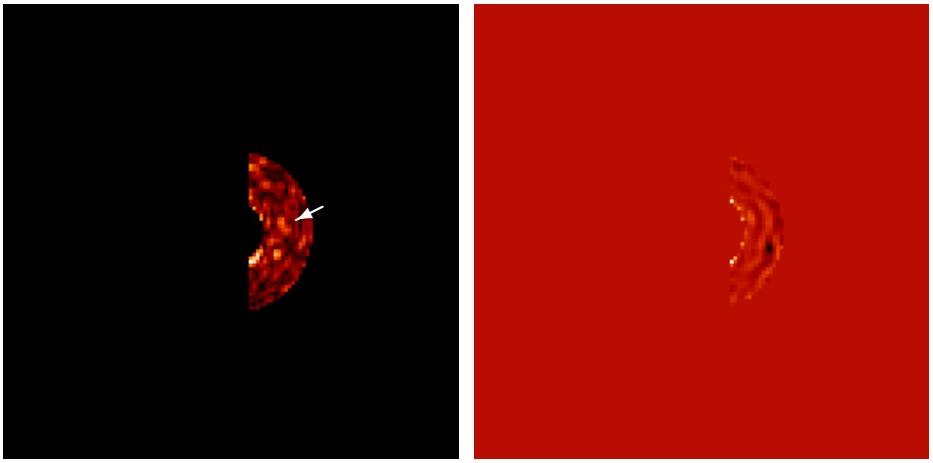

(a) Single monochromatic image before CSD, with DM

(b) Single broadband image after CSD, with DM

Figure 32: Single images before and after CSD. (a) The single monochromatic image is taken at the central wavelength λ_0. (b) The single broadband image is computed by collapsing the cube of monochromatic images after CSD and after rescaling.

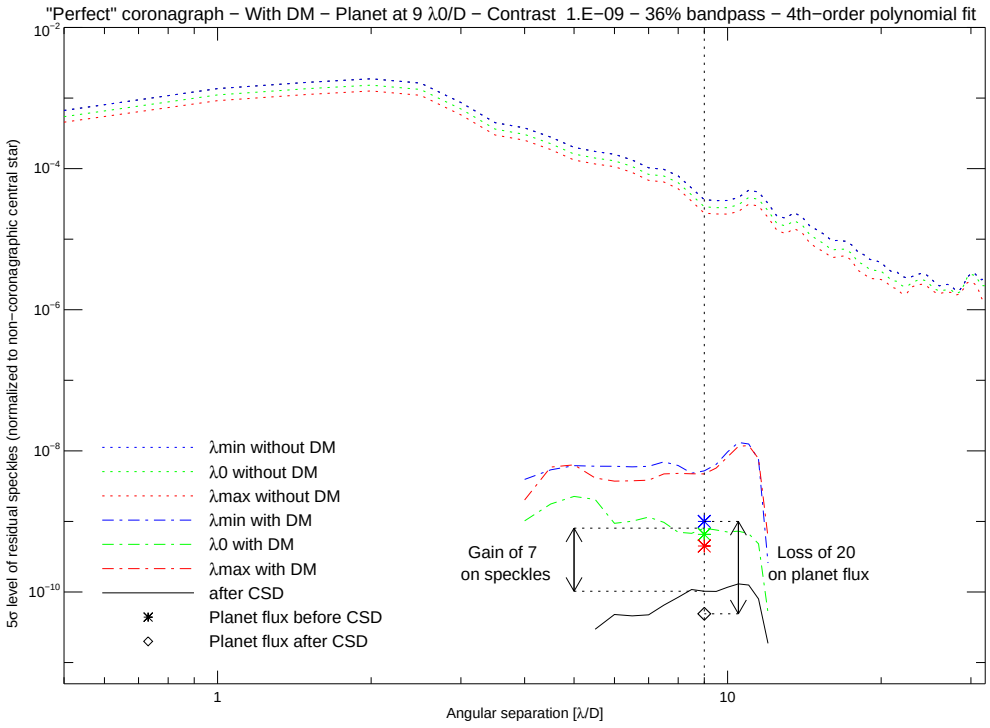

Figure 33: 5σ levels of residual speckles normalized to the non-coronagraphic central star for 36% bandpass. The dotted lines represent the contrast curves of the data cube of speckles without DM for the minimum (blue), central (green) and maximum (red) wavelengths. The dashed lines represent the contrast curves of the data cube of speckles with one DM for the minimum (blue), central (green) and maximum (red) wavelengths. The black solid line represents the contrast curve after CSD of the single broadband image. Asterisk-shaped data represent the flux of the planet before CSD for the minimum (blue), central (green) and maximum (red) wavelengths. Diamond-shaped data represent the flux of the planet after CSD of the single broadband image with the planet only. We emphasize that levels of contrast such as 10^{-10} might not be achieved in practice by WFIRST-AFTA because of other limiting factors not included in the simulations presented here.

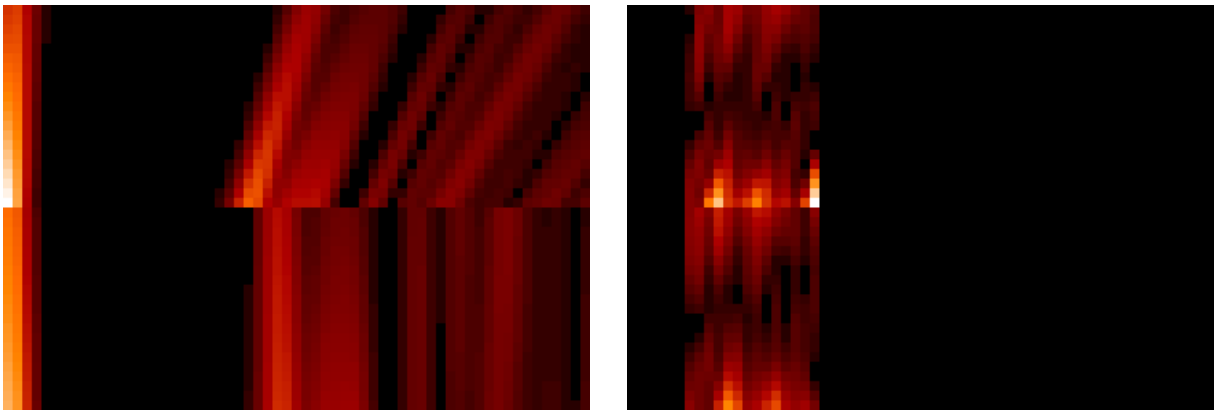

(a) Out of the dark zone (b) In the dark zone

Figure 34: Spatial and spectral evolutions of pixel intensity with the wavelength [top] before and [bottom] after rescaling - with DM. (a) Without mask, (b) with a mask to see what's happening in the dark zone.

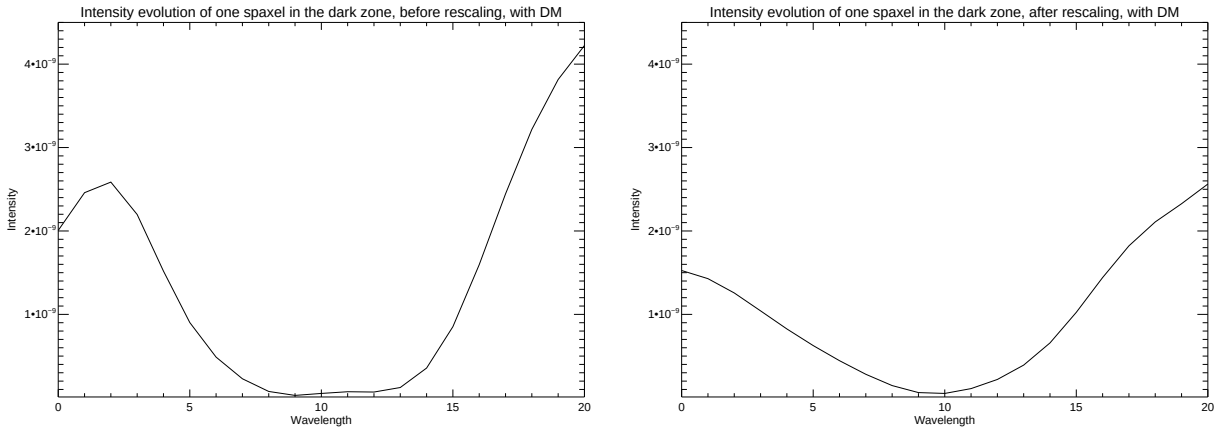

(a) Before rescaling (b) After rescaling

Figure 35: Spectral evolution of a speckle pixel intensity with the wavelength (a) before and (b) after rescaling with DM.

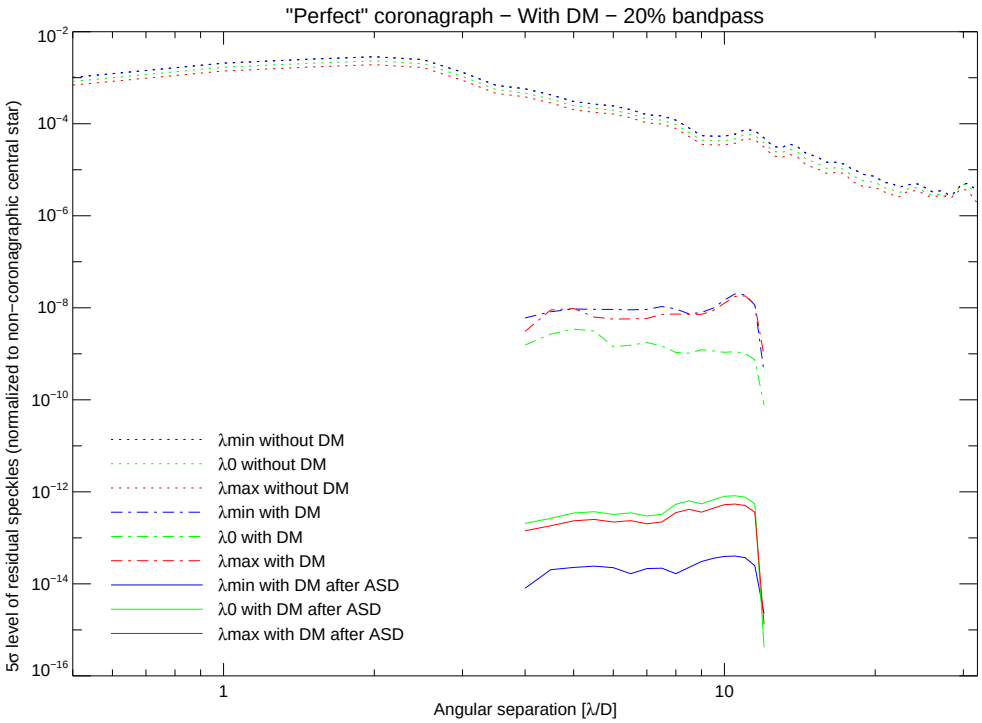

(a) Adapted Spectral Deconvolution (ASD) with a 10th-order polynomial fit with DM

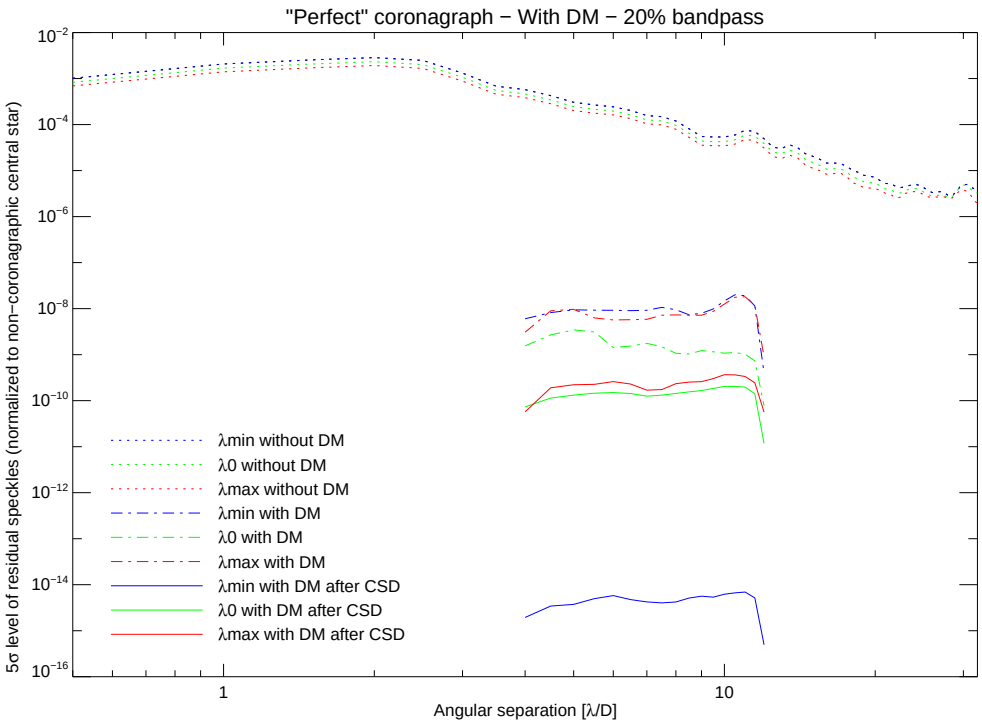

(b) Classical Spectral Deconvolution (CSD) with a 10th-order polynomial fit with DM

Figure 36: 5σ levels of residual speckles normalized to the non-coronagraphic central star for the 36% bandpass. The dotted lines represent the contrast curves of the data cube of speckles without DM for the minimum (blue), central (green) and maximum (red) wavelengths. The dashed lines represent the contrast curves of the data cube of speckles with one DM for the minimum (blue), central (green) and maximum (red) wavelengths. The solid lines represents the contrast curve after (a) ASD or (b) CSD of the single broadband image for the minimum (blue), central (green) and maximum (red) wavelengths. We emphasize that levels of contrast such as 10^{-10} and lower might not be achieved in practice by WFIRST-AFTA because of other limiting factors not included in the simulations presented here.

III CONCLUSIONS AND FUTURE TASKS

6 CONCLUSION

Coronagraphic imaging at 10^{-9} of contrast is a challenge. A factor of 10 is expected to come from post-processing and some techniques have been very successful at lower levels of contrast. Applying these techniques directly on AFTA-like simulated images is not straightforward and this reasserts the importance of studying them a early in the mission planning. This work is a necessary long-term effort to leverage the astronomical return as soon as the mission of the AFTA coronagraph begins. For the first time we apply some methods of PSF subtraction to WFIRST-AFTA like simulated coronagraphic images. We quantify the relative contrast gain provided by post-processing under various assumptions for spacecraft+telescope+instrument thermal models and observing scenarios. It is by no means a reflection upon the validity of these models in terms of absolute contrast. Two different types of diversity are exploited to process the images: the RDI and the SDI.

We compare two different methods using RDI: the classical PSF subtraction and KLIP, the latter having been very successful in the past in the context of high contrast imaging. Depending on the test case, we made different observations. In the case of OS1 time series data, the classical PSF subtraction performs as well as KLIP with a small number of modes. This observation is surprising with respect to the results that have already been obtained with KLIP for real data. After more in-depth studies, we conclude that this is probably due to the statistics of the data. For the coma distribution, we observed that KLIP is less sensitive to bigger amounts of coma than the classical PSF subtraction. In the case of HBLC OS3 time series data, even with a small number of KLIP modes, KLIP performs better than the classical PSF subtraction. For this data set, the number of images provided is not sufficient to make good statistics, but we know that the thermal model is different. An interesting result here is that the KLIP behavior seems to depend strongly on the thermal model used to simulate the data. The OS3 time series data are more recent and theoretically more accurate. We report gains in contrast from 20 to 140 with 88 KLIP modes for noiseless data simulated with a SPC coronagraph and contrast gains from 5 to 30 with 8 KLIP modes for noiseless data simulated with a HLC coronagraph and with the LOWFC, even at separations under $5\lambda/D$.

Classical spectral deconvolution has been specifically conceived to process multi-spectral images as it uses spectral diversity. But we find it is finally useless in this form for WFIRST-AFTA for one reason: it is not possible to disentangle a planet signal from the speckles if the model of the speckles that we have also fits the planet. This is the case for classical spectra deconvolution, which does not model the presence of the planet. For this reason, some of the most

promising methods for WFIRST-AFTA today are the PCA-based techniques using RDI such as KLIP. This is why we will study the performance of KLIP with priority, in particular for spectrum extraction. If it is not sufficient to reach the required gain of 10, we may want to exploit spectral diversity offered by the IFS as well. But in this case, we would need different kinds of methods with a good model of the speckle evolution with the wavelength and a model of the planet.

7 PERSPECTIVES

This work has already opened up numerous perspectives. Among them, the future tasks include:

- Developing quantitative metrics for detection;
- Apply forward modeling to estimate photometry and astrometry;
- Conclude the correlation study once we have sufficient data for the OS3 HBLC time series;
- Using 61 Uma as a reference star instead of 47 Uma, to estimate the sensitivity to different star spectra;
- Extracting spectra from the OS1 SPC time series;
- Studying the performances of KLIP in exploiting the spectral diversity offered by the IFS;
- Exploring the possible performance improvement from exploiting the Angular Differential Imaging (ADI).

8 ACKNOWLEGMENTS

This WFIRST-AFTA study was carried out at Space Telescope Science Institute (STScI) under subcontract No. 1506553, funded by the Jet Propulsion Laboratory (JPL), which is managed for NASA by the California Institute of Technology. The authors are grateful to John Krist and Mamadou N'Diaye for providing simulations used in this study, and to Bertrand Mennesson and John Krist for helpful discussions.

9 ACRONYM LIST

AFTA - Astrophysics Focused Telescope Assets
ALICE - Archival Legacy Investigations of Circumstellar Environments
AO - Adaptive Optics
APRC - APodized Roddier Coronagraph

CSD - Classical Spectral Deconvolution
DM - Deformable Mirror
E-ELT - European-Extremely Large Telescope
EFC - Electric Field Conjugation
GPI - Gemini Planet Imager
HLC - Hybrid Lyot Coronagraph
HBLC - Hybrid BandLimited Coronagraph
HST- Hubble Space Telescope
IFS - Integral Field Spectrograph
IWA - Inner Working Angle
JPL - Jet Propulsion Laboratory
KLIP - Karhunen-Loève Image Projection Algorithm
LOCI - Locally Optimized Combination of Images
LOWFC - Low-Order Wavefront Control
LOWFSC - Low-Order Wavefront Sensing and Control
NaCo - Nasmyth Adaptive Optics System (NAOS) Near-Infrared Imager and Spectrograph (CONICA)
NICMOS - Near Infrared Camera and Multi-Object Spectrometer
OS - Observing Sequence
OWA - Outer Working Angle
PCA - Principal Component Analysis
PSF - Point Spread Function
RDI - Reference Star Differential Imaging
SD - Spectral Deconvolution
SINFONI - Spectrograph for INtegral Field Observations in the Near Infrared
SPC - Shaped Pupil Coronagraph
SPHERE - Spectro-Polarimetric High-contrast Exoplanet REsearch
STScI - Space Telescope Science Institute
VLT - Very Large Telescope
WFC3 - Wide Field Camera 3
WFIRST - Wide Field InfraRed Survey Telescope

IV APPENDIX

10 WHAT HAPPENS IF WE RUN A KLIP ANALYSIS USING ALL INDIVIDUAL SCIENCE IMAGES RATHER THAN THEIR SUM?

To answer this question, we perform several KLIP reductions illustrated by figures 39 and 40:

- In the reduction #1, KLIP is directly applied on the collapsed science images for the polarization X
- In the reduction #2, KLIP is directly applied on the collapsed science images for the polarization Y
- In the reduction #3: KLIP is applied first on individual science images for the polarization X. The images are then collapsed.
- In the reduction #4: KLIP is applied first on individual science images for the polarization Y. The images are then collapsed.

A similar set of reduction is done for noisy images, yielding the reductions #1n, #2n, #3n and #4n.

Reduction #1: KLIP directly applied on collapsed science images - Polarization X

Load cubeData1 = ”OS1.0_47_Uma_HLC_polX_sequence_noiseless.fits”
Load cubeRef1 = ”OS1.0_beta_Uma_HLC_polX_sequence_noiseless.fits”
tmp1 = Collapse(cubeData1)
Result1 = KLIP(tmp1,cubeRef1)

Reduction #2: KLIP directly applied on collapsed science images - Polarization Y

Load cubeData2 = ”OS1.0_47_Uma_HLC_polY_sequence_noiseless.fits”
Load cubeRef2 =”OS1.0_beta_Uma_HLC_polY_sequence_noiseless.fits”
tmp2 = Collapse cubeData2
Result2 = KLIP(tmp2,cubeRef2)

Reduction #3: KLIP applied on individual science images, then collapsed - Polarization X

Load cubeData1= ”OS1.0_47_Uma_HLC_polX_sequence_noiseless.fits”
Load cubeRef1 = ”OS1.0_beta_Uma_HLC_polX_sequence_noiseless.fits”
tmp3_i = KLIP(cubeData1a_i,cubeRef1) with i the i-th image of the data cube
Result3 = Collapse(tmp3)

Reduction #4: KLIP applied on individual science images, then collapsed - Polarization Y

Load cubeData2=”OS1.0_47_Uma_HLC_polY_sequence_noiseless.fits”
Load cubeRef2 = ”OS1.0_beta_Uma_HLC_polY_sequence_noiseless.fits”
tmp4_i = KLIP(cubeData2_i,cubeRef2) with i the i-th image of the data cube
Result4 = Collapse(tmp4)

Reduction #1n: KLIP directly applied on collapsed science images - Polarization X - With noise

Load cubeData1n = ”OS1.0_47_Uma_HLC_polX_sequence.fits”
Load cubeRef1n = ”OS1.0_beta_Uma_HLC_polX_sequence.fits”
tmp1n = Collapse(cubeData1n)
Result1n = KLIP(tmp1n,cubeRef1n)

Reduction #2n: KLIP directly applied on collapsed science images - Polarization Y - With noise

Load cubeData2n = ”OS1.0_47_Uma_HLC_polY_sequence.fits”
Load cubeRef2n =”OS1.0_beta_Uma_HLC_polY_sequence.fits”
tmp2n = Collapse cubeData2n
Result2n = KLIP(tmp2n,cubeRef2n)

Reduction #3n: KLIP applied on individual science images, then collapsed - Polarization X - With noise

Load cubeData1n= ”OS1.0_47_Uma_HLC_polX_sequence.fits”
Load cubeRef1n = ”OS1.0_beta_Uma_HLC_polX_sequence.fits”
tmp3n_i = KLIP(cubeData1n_i,cubeRef1n) with i the i-th image of the data cube
Result3n = Collapse(tmp3n)

Reduction #4n: KLIP applied on individual science images, then collapsed - Polarization Y - With noise

Load cubeData2n=”OS1.0_47_Uma_HLC_polY_sequence.fits”
Load cubeRef2n = ”OS1.0_beta_Uma_HLC_polY_sequence.fits”
tmp4n_i = KLIP(cubeData2n_i,cubeRef2n) with i the i-th image of the data cube
Result4n = Collapse(tmp4n)

There is no difference between Reduction #1 and Reduction #3, between Reduction #2 and Reduction #4 (cf. simulation results in Fig. 37 and 38). We can make exactly the same observation for the noisy data. It is easy to demonstrate analytically that it is a linear process:

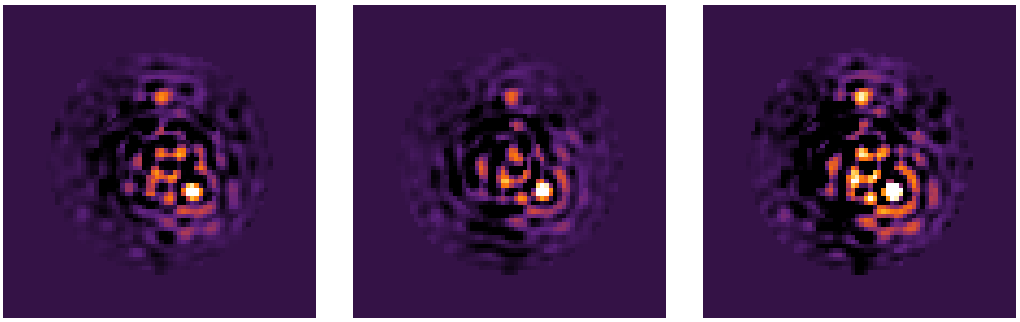

(a) KLIP directly applied on collapsed science images - Reduction #1 and Reduction #2

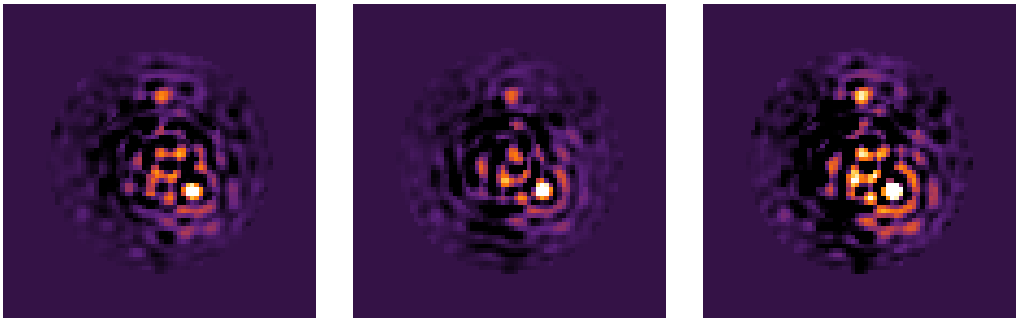

(b) KLIP applied on individual science images, then collapsed - Reduction #3 and Reduction #4

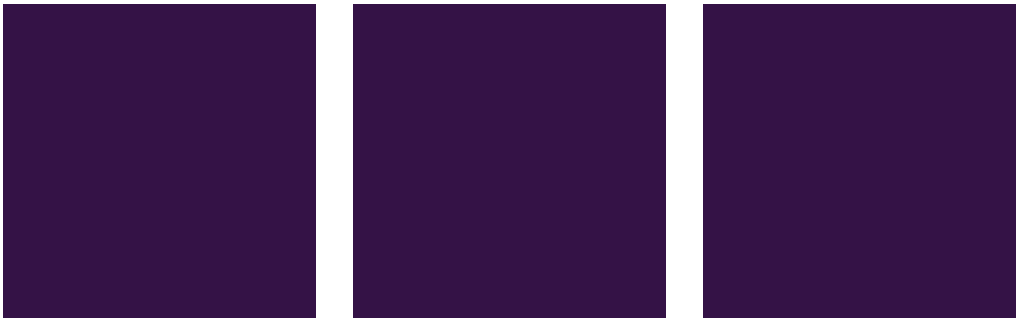

(c) Difference between the two results

Figure 37: KLIP analysis using either the sum of individual science images or all individual science images without noise. Illustration with 4 KLIP modes. [Left] X polarization, [center] Y polarization, [right] X+Y polarization

$$
\begin{aligned}
\hat{I}_{\Psi_0}(n) &= \sum_{k=1}^{K_klip} \left|T, Z_k^{KL}\right|_S Z_k^{KL}(n) \\
F(n) &= T(n) - \hat{I}_{\Psi_0}(n) \\
\sum F(n) &= \sum_j T_j(n) - \sum_j \hat{I}_{\Psi_0}(n)_j \\
&= \sum_j T_j(n) - \sum_j \sum_{k=1}^{K_klip} \left|T_j, Z_k^{KL}\right|_S Z_k^{KL}(n) \\
&= \sum_j T_j(n) - \sum_j \sum_k \sum_i T_i j Z_k^{KL} Z_k^{KL}(n) \\
&= \sum_j T_j(n) - \sum_j \sum_k \left[\sum_i T_{ij}\right] Z_{kj} Z_k^{KL}(n)
\end{aligned}
$$

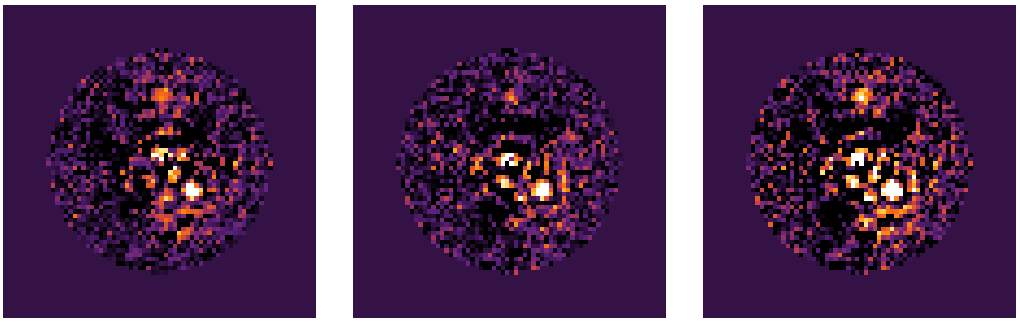

(a) KLIP directly applied on collapsed science images - Reduction #1N and Reduction #2N

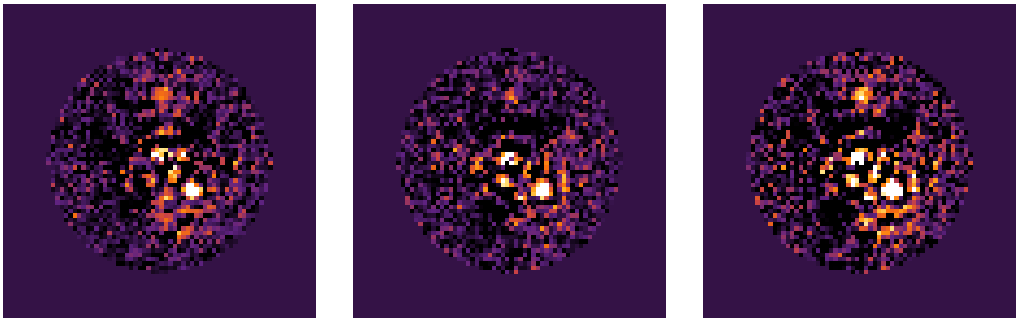

(b) KLIP applied on individual science images, then collapsed - Reduction #3N and Reduction #4N

(c) Difference between the two results

Figure 38: KLIP analysis using either the sum of individual science images or all individual science images with noise. Illustration with 4 KLIP modes. [Left] X polarization, [center] Y polarization, [right] X+Y polarization

This shows that the analysis using all individual science images is exactly the same thing as analyzing directly their sum. The second option being faster that the first one, we have used it in all the analysis of this report.

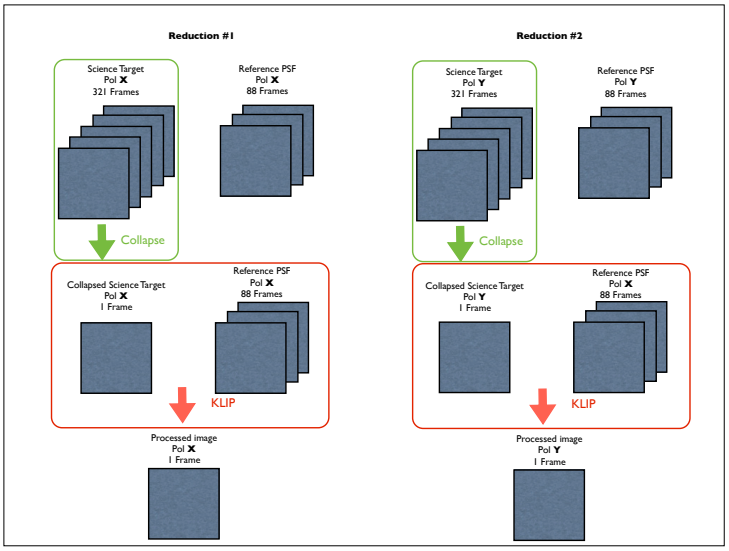

Figure 39: Illustration of Reductions #1 and #2

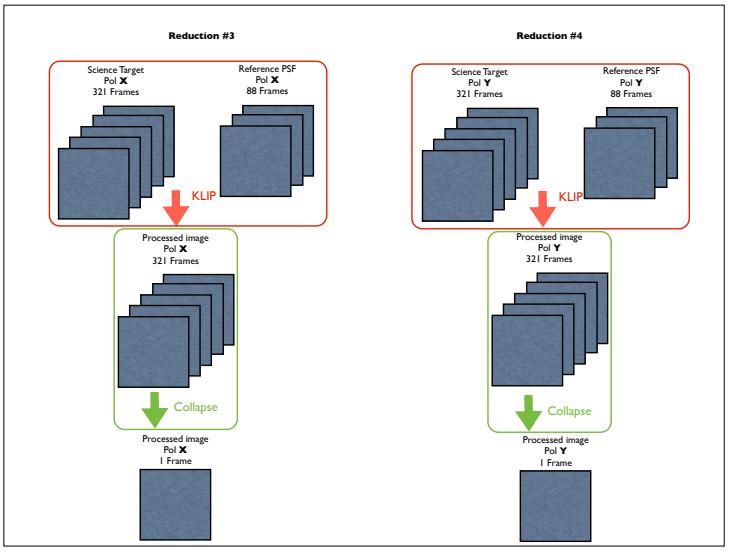

Figure 40: Illustration of Reductions #3 and #4

11 WHAT IF ONLY ONE POLARIZATION IS OPTIMIZED INSTEAD OF THE 2 JOINTLY? DOES THAT PROVIDE BETTER POST-PROCESSING PERFORMANCE IN THE END?

To answer to this question, we perform several KLIP reductions illustrated by figure 41 for both noiseless and noisy images:

- In the reduction #5, KLIP is directly applied on the collapsed science images for the polarization X+Y
- The reduction #5 can be compared directly to the sum of reductions #1 and #2 for polarization X and Y respectively that we performed previously.

Reduction #5: KLIP directly applied on collapsed science images X+Y polarizations

Load cubeData1 = ”OS1.0_47_Uma_HLC_polX_sequence_noiseless.fits”
Load cubeData2 = ”OS1.0_47_Uma_HLC_polY_sequence_noiseless.fits”
Load cubeRef1 = ”OS1.0_beta_Uma_HLC_polX_sequence_noiseless.fits”
Load cubeRef2 = ”OS1.0_beta_Uma_HLC_polY_sequence_noiseless.fits”
ScienceCubeXYnoiseless = cubeData1 + cubeData2 ReferenceCubeXYnoiseless = cubeRef1 + cubeRef2 tmp5 = Collapse(ScienceCubeXYnoiseless)
Result5 = KLIP(tmp5,ReferenceCubeXYnoiseless)

Reduction #5n: KLIP directly applied on collapsed science images X+Y polarizations - With noise

Load cubeData1n = ”OS1.0_47_Uma_HLC_polX_sequence.fits”
Load cubeData2n = ”OS1.0_47_Uma_HLC_polY_sequence.fits”
Load cubeRef1n = ”OS1.0_beta_Uma_HLC_polX_sequence.fits”
Load cubeRef2n = ”OS1.0_beta_Uma_HLC_polY_sequence.fits”
ScienceCubeXY= cubeData1 + cubeData2 ReferenceCubeXY = cubeRef1 + cubeRef2
tmp5n = Collapse(ScienceCubeXY)
Result5n = KLIP(tmp5,ReferenceCubeXY)

We observe a tiny difference which is probably explained by the fact that we use both CubeRefX and CubeRefY to process CubeDataX+CubeDataY (a), instead of using only CubeRefX to process CubeDataX and CubeRefY to process CubeDataY (b). But the performance is the same (cf. contrast curves in Fig. 43). We conclude that there is not significative difference in term of post-processing performance.

12 COMPARISON BETWEEN INITIAL AND COMA DISTRIBUTIONS

In this appendix, we compare the initial and coma distributions. The initial distribution refers to the first OS1 time series that we received in October 2014. The coma distribution refers to the OS1 time series with different amounts of coma received in February 2015. The figure 44 shows the results of the reductions for the initial and coma distributions.

By reducing both initial and coma distributions, we have noticed a difference in the results. We have also identified 4 planet candidates on the new distribution but one candidate (candidate #4b) is different between the two distributions (cf. Figure 7). This new planet is visible both on the classical PSF reduction and KLIP reduction with 4 modes.

After clarification with John Krist, the new distribution consists in new files for the X polarization channel optimized for X only and thus have better raw contrast (about 5x better). We can see it clearly if we compare the two long exposure raw images of the initial and coma distribution on the top left and bottom left of the figure respectively. On the contrary, the old

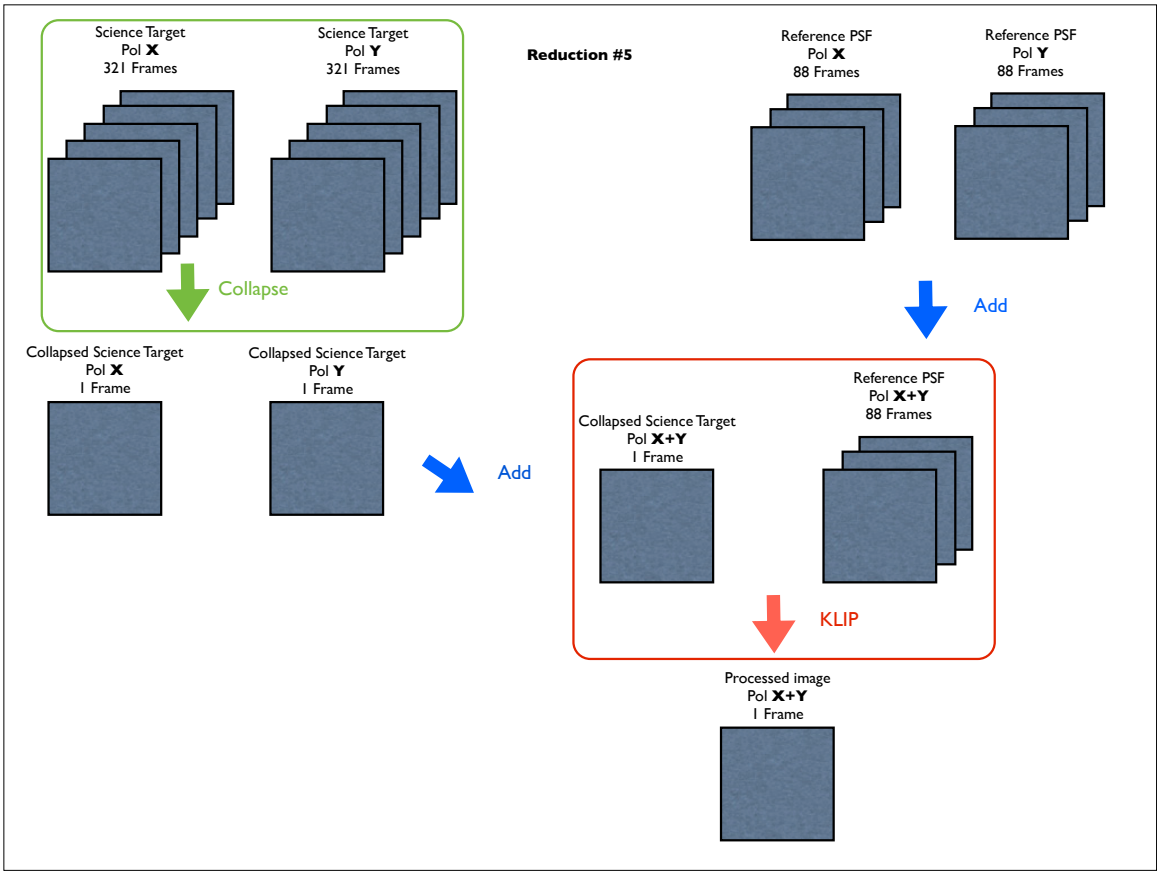

Figure 41: Illustration of Reduction #5

OS1 data includes both X and Y polarization channels for the X+Y optimized dark hole.

To conclude on this comparison, it is better to optimize the dark hole on X rather than X+Y for the X polarization channel. The reason is that the post-processing seems to work better for the two methods for the coma distribution. The candidate #4 which has been previously identified as a candidate is not visible anymore on these reduced data whereas another planet candidate (candidate #4b) appears clearly for the smallest amount of coma. And this candidate, as well are the candidates #1 and #2, turned out the be real synthetic planets injected by John Krist.

13 COMPARISON FOR DIFFERENT KLIP SEARCH ZONES

We reduced the OS1 times series simulated with an HLC coronagraph with different amounts of coma a second time with 7 search zones for KLIP instead of one (cf. Figure 45). This time, we represent the reduction with only 11 modes instead of 88. We noticed a small improvement for the residual level but nothing critical with respect to the detection.

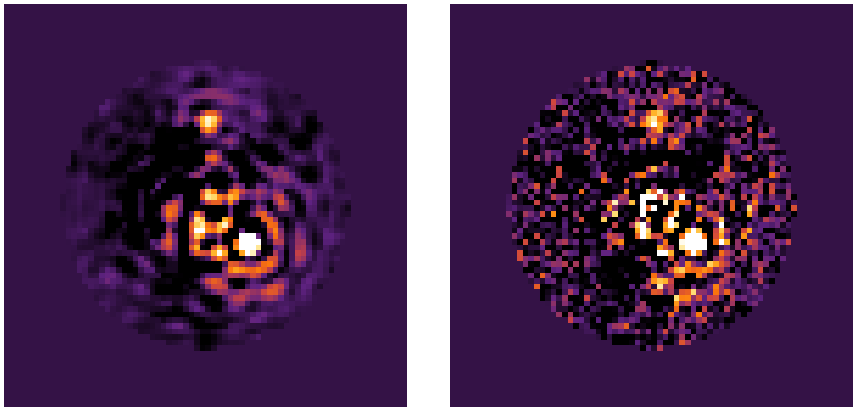

(a) KLIP directly applied on collapsed science images X+Y polarizations - Reduction #5 and Reduction #5N

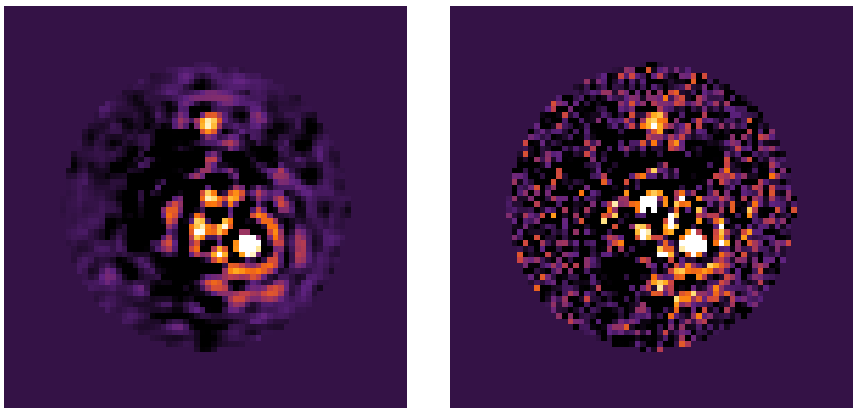

(b) KLIP applied on individual polarized science images X and Y, then collapsed - Reduction #1 + Reduction #2 and Reduction #1N + Reduction #2N

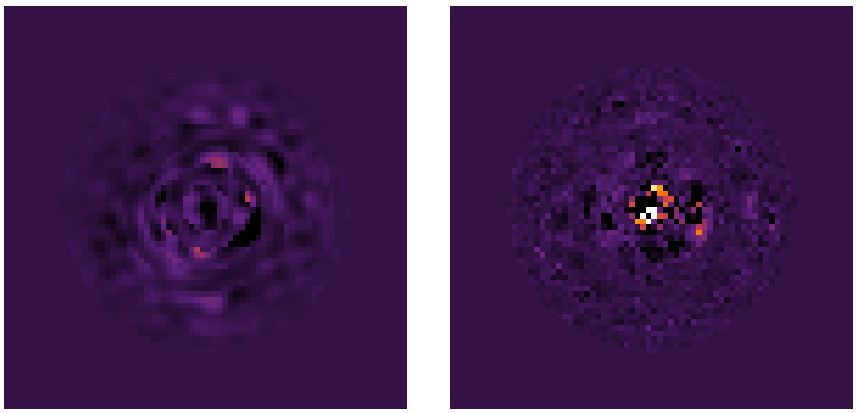

(c) Difference between the two results

Figure 42: KLIP analysis using either the sum polarized science images or individual polarized science images without and with noise. Illustration with 4 KLIP modes. [Left] With noise, [right] without noise

References

[1] D. Spergel, N. Gehrels, J. Breckinridge, M. Donahue, A. Dressler, B. S. Gaudi, T. Greene, O. Guyon, C. Hirata, J. Kalirai, N. J. Kasdin, W. Moos, S. Perlmutter, M. Postman,

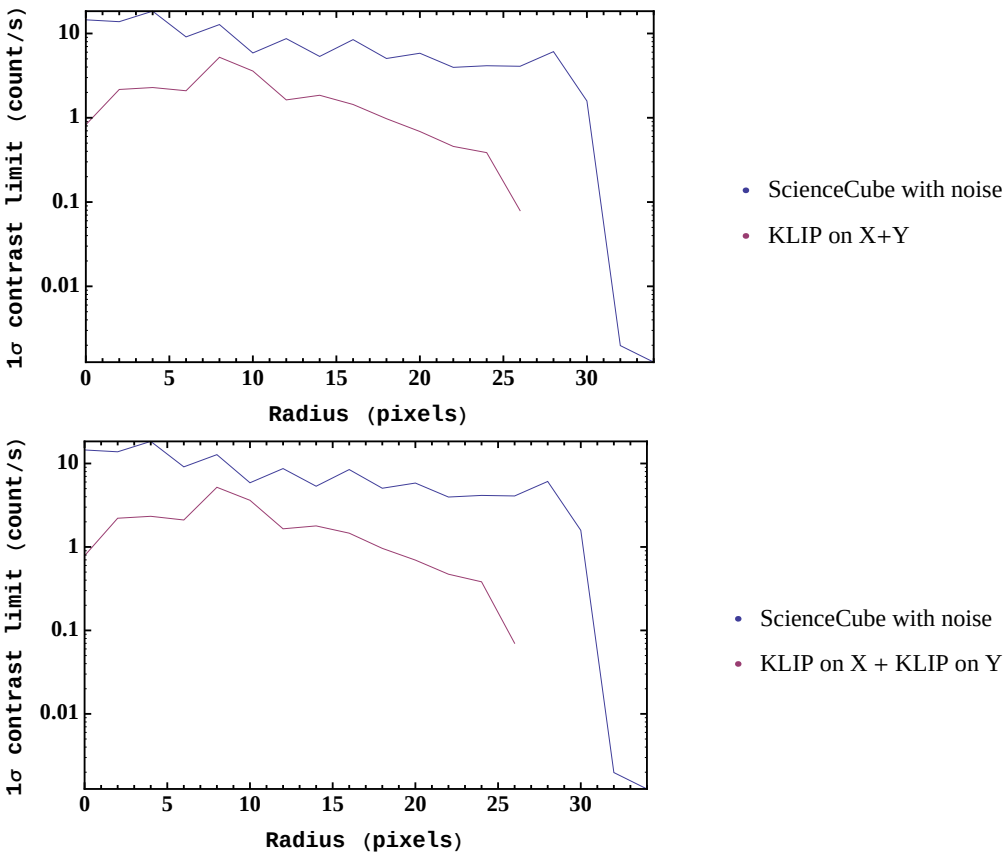

Figure 43: KLIP analysis using either the sum polarized science images or individual polarized science images without and with noise - contrast curves. Illustration with 4 KLIP modes. [Left] With noise, [right] without noise

B. Rauscher, J. Rhodes, Y. Wang, D. Weinberg, J. Centrella, W. Traub, C. Baltay, J. Colbert, D. Bennett, A. Kiessling, B. Macintosh, J. Merten, M. Mortonson, M. Penny, E. Rozo, D. Savransky, K. Stapelfeldt, Y. Zu, C. Baker, E. Cheng, D. Content, J. Dooley, M. Foote, R. Goullioud, K. Grady, C. Jackson, J. Kruk, M. Levine, M. Melton, C. Peddie, J. Ruffa, and S. Shaklan. Wide-Field InfraRed Survey Telescope-Astrophysics Focused Telescope Assets WFIRST-AFTA Final Report. *ArXiv e-prints*, May 2013.

[2] D. Spergel and J. Kasdin. A Shaped Pupil Coronagraph: A Simpler Path towards TPF. In *American Astronomical Society Meeting Abstracts*, volume 33 of *Bulletin of the American Astronomical Society*, page 1431, December 2001.

[3] N. J. Kasdin, R. J. Vanderbei, D. N. Spergel, and M. G. Littman. Extrasolar Planet Finding via Optimal Apodized-Pupil and Shaped-Pupil Coronagraphs. *Astrophys. J.*, 582:1147–1161, January 2003.

[4] A. Carlotti, N. J. Kasdin, and R. J. Vanderbei. Shaped pupil coronagraphy with WFIRST-AFTA. In *Society of Photo-Optical Instrumentation Engineers (SPIE) Conference Series*, volume 8864 of *Society of Photo-Optical Instrumentation Engineers (SPIE) Conference Series*, page 10, September 2013.

[5] D. C. Moody and J. T. Trauger. Hybrid Lyot coronagraph masks and wavefront control for

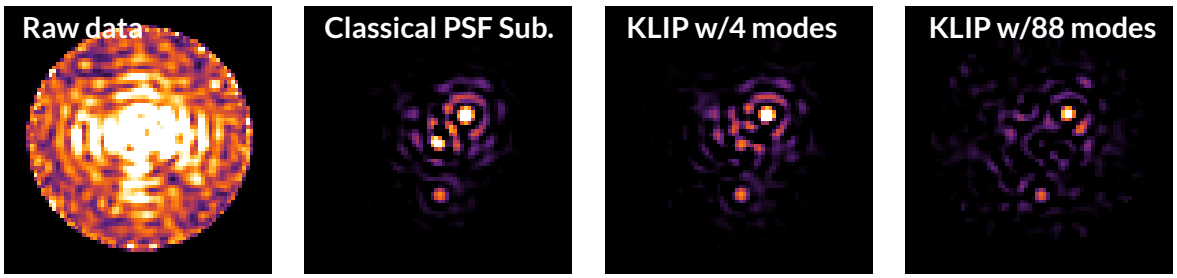

(a) Initial distribution

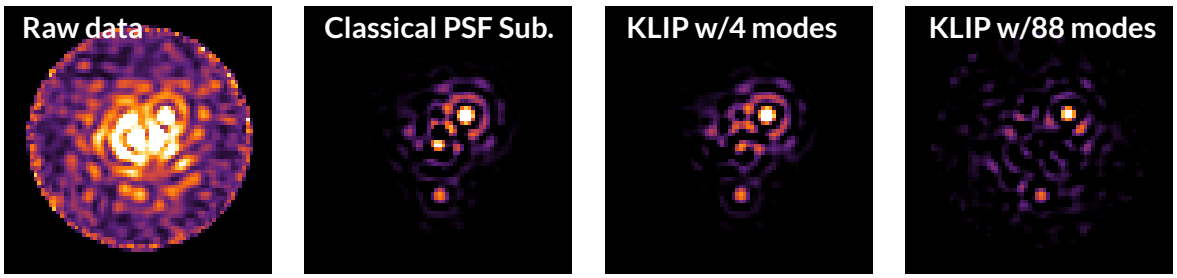

(b) Coma distribution

Figure 44: **Broadband HLC time series**. Comparison between initial and coma distribution. Top: (a) initial distribution. Bottom: (b) coma distribution. From left to right with same dynamic: Raw image (long exposure), image processed with classical PSF subtraction, image processed with KLIP 4 modes and image processed with KLIP 88 modes.

improved spectral bandwidth and throughput. In *Society of Photo-Optical Instrumentation Engineers (SPIE) Conference Series*, volume 6693 of *Society of Photo-Optical Instrumentation Engineers (SPIE) Conference Series*, page 1, September 2007.

[6] J. T. Trauger, B. Gordon, and D. Moody. The Hybrid Lyot Coronagraph for the Imaging of Exoplanet Systems with the AFTA telescope. In *American Astronomical Society Meeting Abstracts #223*, volume 223 of *American Astronomical Society Meeting Abstracts*, page 109.03, January 2014.

[7] J. E. Krist. End-to-end numerical modeling of AFTA coronagraphs. In *Society of Photo-Optical Instrumentation Engineers (SPIE) Conference Series*, volume 9143 of *Society of Photo-Optical Instrumentation Engineers (SPIE) Conference Series*, page 0, August 2014.

[8] A. Give'on, B. Kern, S. Shaklan, D. C. Moody, and L. Pueyo. Broadband wavefront correction algorithm for high-contrast imaging systems. In *Society of Photo-Optical Instrumentation Engineers (SPIE) Conference Series*, volume 6691 of *Society of Photo-Optical Instrumentation Engineers (SPIE) Conference Series*, page 0, September 2007.

[9] J. K. Wallace, S. Rao, R. M. Jensen-Clem, and G. Serabyn. Phase-shifting Zernike interferometer wavefront sensor. In *Society of Photo-Optical Instrumentation Engineers (SPIE)*

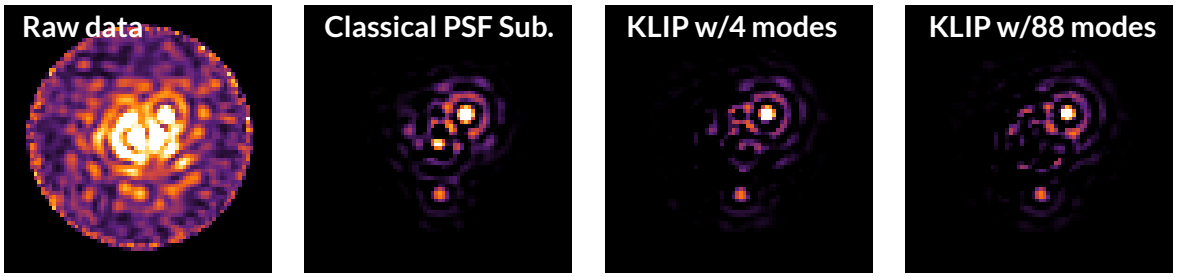

(a) Coma x1

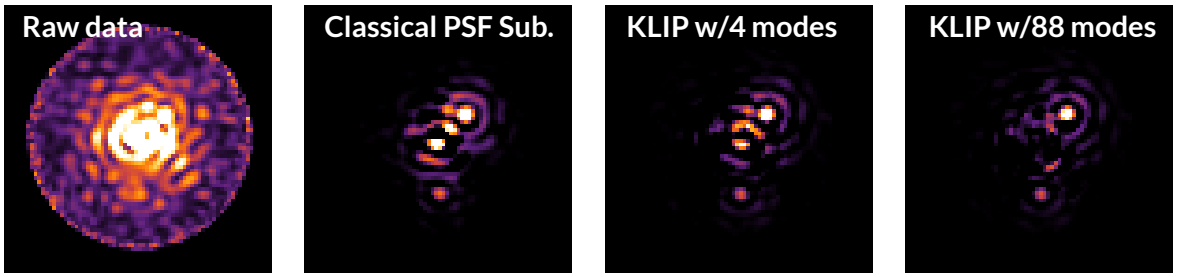

(b) Coma x2

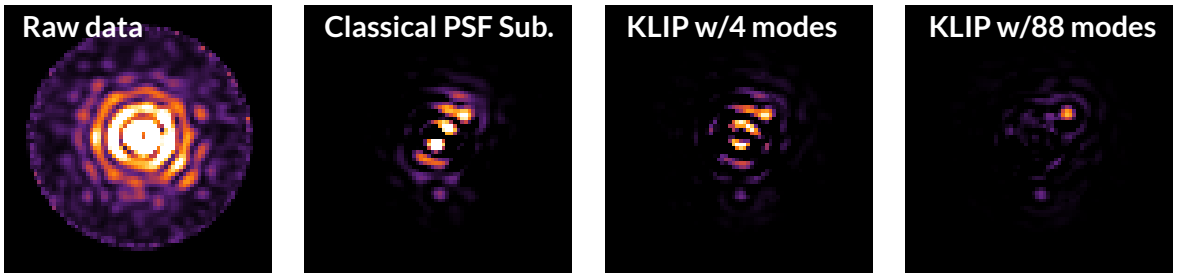

(c) Coma x4

Figure 45: **Broadband HLC time series**. Comparison for different amounts of coma. Top: reference amount of coma (coma x1), Center: reference amount of coma multiplied by 2 (coma x2), Bottom: reference amount of coma multiplied by 4 (coma x4). From left to right with same dynamic: Raw image (long exposure), Image processed with Classical PSF subtraction, image processed with KLIP 4 modes and image processed with KLIP 11 modes.

Conference Series, volume 8126 of *Society of Photo-Optical Instrumentation Engineers (SPIE) Conference Series*, September 2011.

[10] D. Mawet, L. Pueyo, P. Lawson, L. Mugnier, W. Traub, A. Boccaletti, J. T. Trauger, S. Gladysz, E. Serabyn, J. Milli, R. Belikov, M. Kasper, P. Baudoz, B. Macintosh, C. Marois, B. Oppenheimer, H. Barrett, J.-L. Beuzit, N. Devaney, J. Girard, O. Guyon, J. Krist, B. Mennesson, D. Mouillet, N. Murakami, L. Poyneer, D. Savransky, C. Vérinaud, and J. K. Wallace. Review of small-angle coronagraphic techniques in the wake of ground-based second-generation adaptive optics systems. In *Society of Photo-Optical Instrumentation Engineers (SPIE) Conference Series*, volume 8442 of *Society of Photo-Optical Instrumentation Engineers (SPIE) Conference Series*, page 4, September 2012.

[11] D. Lafrenière, C. Marois, R. Doyon, D. Nadeau, and É. Artigau. A New Algorithm for Point-Spread Function Subtraction in High-Contrast Imaging: A Demonstration with Angular Differential Imaging. *Astrophys. J.*, 660:770–780, May 2007.

[12] R. Soummer, L. Pueyo, and J. Larkin. Detection and Characterization of Exoplanets and Disks Using Projections on Karhunen-Loève Eigenimages. *Astrophys. J. Lett.*, 755:L28, August 2012.

[13] A. Amara and S. P. Quanz. PYNPOINT: an image processing package for finding exoplanets. *Mon. Not. R. Astron. Soc.*, 427:948–955, December 2012.

[14] A. Rajan, T. Barman, R. Soummer, L. Pueyo, J. Patience, J. Brendan Hagan, B. Macintosh, C. Marois, and Q. M. Konopacky. Detection and characterization of the atmospheres of the HR 8799 b and c planets with high contrast HST/WFC3 imaging. In *American Astronomical Society Meeting Abstracts*, volume 225 of *American Astronomical Society Meeting Abstracts*, page #323.07, January 2015.

[15] R. Soummer, M. D. Perrin, L. Pueyo, É. Choquet, C. Chen, D. A. Golimowski, J. Brendan Hagan, T. Mittal, M. Moerchen, M. N'Diaye, A. Rajan, S. Wolff, J. Debes, D. C. Hines, and G. Schneider. Five Debris Disks Newly Revealed in Scattered Light from the Hubble Space Telescope NICMOS Archive. *Astrophys. J. Lett.*, 786:L23, May 2014.

[16] E. Choquet, J. B. Hagan, L. Pueyo, M. D. Perrin, D. C. Hines, C. Chen, G. Schneider, J. Debes, D. Golimowski, N. Reid, T. Mittal, M. Moerchen, M. N'Diaye, A. Rajan, S. Lonsdale, and R. Soummer. Archival Legacy Investigation of Circumstellar Environments using KLIP algorithm on HST NICMOS coronagraphic data. In M. Booth, B. C. Matthews, and J. R. Graham, editors, *IAU Symposium*, volume 299 of *IAU Symposium*, pages 30–31, January 2014.

[17] L. Pueyo, R. Soummer, J. Hoffmann, R. Oppenheimer, J. R. Graham, N. Zimmerman, C. Zhai, J. K. Wallace, F. Vescelus, A. Veicht, G. Vasisht, T. Truong, A. Sivaramakrishnan, M. Shao, L. C. Roberts, Jr., J. E. Roberts, E. Rice, I. R. Parry, R. Nilsson, S. Luszcz-Cook, T. Lockhart, E. R. Ligon, D. King, S. Hinkley, L. Hillenbrand, D. Hale, R. Dekany, J. R. Crepp, E. Cady, R. Burruss, D. Brenner, C. Beichman, and C. Baranec. Reconnaissance of the HR 8799 Exosolar System II: Astrometry and Orbital Motion. *ArXiv e-prints*, September 2014.

[18] M. D. Perrin, G. Duchene, M. Millar-Blanchaer, M. P. Fitzgerald, J. R. Graham, S. J. Wiktorowicz, P. G. Kalas, B. Macintosh, B. Bauman, A. Cardwell, J. Chilcote, R. J. De Rosa, D. Dillon, R. Doyon, J. Dunn, D. Erikson, D. Gavel, S. Goodsell, M. Hartung, P. Hibon, P. Ingraham, D. Kerley, Q. Konapacky, J. E. Larkin, J. Maire, F. Marchis, C. Marois, T. Mittal, K. M. Morzinski, B. R. Oppenheimer, D. W. Palmer, J. Patience, L. Poyneer, L. Pueyo, F. T. Rantakyrö, N. Sadakuni, L. Saddlemyer, D. Savransky, R. Soummer, A. Sivaramakrishnan,

I. Song, S. Thomas, J. K. Wallace, J. J. Wang, and S. G. Wolff. Polarimetry with the Gemini Planet Imager: Methods, Performance at First Light, and the Circumstellar Ring around HR 4796A. *Astrophys. J.*, 799:182, February 2015.

[19] A. Zurlo, D. Mesa, R. Gratton, R. Claudi, S. Desidera, E. Giro, J.-L. Beuzit, K. Dohlen, D. Mouillet, P. Puget, F. Wildi, M. Feldt, O. Moeller-Nilsson, A. Baruffolo, D. Fantinel, B. Salasnich, M. Kasper, A. Costille, J.-F. Sauvage, A. Vigan, C. Moutou, M. Langlois, J. Antichi, A. Pavlov, N. Zimmerman, and M. Turatto. Methods for the detection and the characterization of low mass companions using the IFS of SPHERE. In *Society of Photo-Optical Instrumentation Engineers (SPIE) Conference Series*, volume 9147 of *Society of Photo-Optical Instrumentation Engineers (SPIE) Conference Series*, page 70, August 2014.

[20] T. Meshkat, M. A. Kenworthy, S. P. Quanz, and A. Amara. Optimized Principal Component Analysis on Coronagraphic Images of the Fomalhaut System. *Astrophys. J.*, 780:17, January 2014.

[21] W. B. Sparks and H. C. Ford. Imaging Spectroscopy for Extrasolar Planet Detection. *Astrophys. J.*, 578:543–564, October 2002.

[22] N. Thatte, R. Abuter, M. Tecza, E. L. Nielsen, F. J. Clarke, and L. M. Close. Very high contrast integral field spectroscopy of ab doradus c: 9-mag contrast at 0.2arcsec without a coronagraph using spectral deconvolution. *Mon. Not. R. Astron. Soc.*, 378:1229–1236, July 2007.

[23] S. Desidera, R. Gratton, R. Claudi, J. Antichi, D. Mesa, M. Turatto, P. Bruno, E. Cascone, V. De Caprio, E. Giro, S. Scuderi, M. Feldt, A. Pavlov, O. Moeller-Nilsson, K. Dohlen, J. L. Beuzit, D. Mouillet, P. Puget, and F. Wildi. Calibration and data reduction for planet detection with SPHERE-IFS. In *Society of Photo-Optical Instrumentation Engineers (SPIE) Conference Series*, volume 7014 of *Presented at the Society of Photo-Optical Instrumentation Engineers (SPIE) Conference*, August 2008.

[24] C. Vérinaud, M. Kasper, J.-L. Beuzit, R. G. Gratton, D. Mesa, E. Aller-Carpentier, E. Fedrigo, L. Abe, P. Baudoz, A. Boccaletti, M. Bonavita, K. Dohlen, N. Hubin, F. Kerber, V. Korkiakoski, J. Antichi, P. Martinez, P. Rabou, R. Roelfsema, H. M. Schmid, N. Thatte, G. Salter, M. Tecza, L. Venema, H. Hanenburg, R. Jager, N. Yaitskova, O. Preis, M. Orecchia, and E. Stadler. System study of EPICS: the exoplanets imager for the E-ELT. In *Society of Photo-Optical Instrumentation Engineers (SPIE) Conference Series*, volume 7736 of *Society of Photo-Optical Instrumentation Engineers (SPIE) Conference Series*, July 2010.

[25] G. S. Salter, N. A. Thatte, M. Tecza, F. Clarke, and M. E. Kasper. Direct Detection of Nearby Habitable Zone Planets Using Slicer Based Integral Field Spectrographs and EPICS on the E-ELT. In N. Haghighipour, editor, *IAU Symposium*, volume 293 of *IAU Symposium*, pages 442–444, April 2014.

[26] G. Salter, N. Thatte, M. Tecza, F. Clarke, C. Verinaud, M. Kasper, and R. Abuter. Exploring high contrast limitations for image slicer-based integral field spectrographs. In *Society of Photo-Optical Instrumentation Engineers (SPIE) Conference Series*, volume 7015 of *Society of Photo-Optical Instrumentation Engineers (SPIE) Conference Series*, July 2008.

[27] A. Vigan, M. Langlois, C. Moutou, and K. Dohlen. Exoplanet characterization with long slit spectroscopy. *Astron. Astrophys.*, 489:1345–1354, October 2008.

[28] L. Pueyo and N. J. Kasdin. Polychromatic Compensation of Propagated Aberrations for High-Contrast Imaging. *Astrophys. J.*, 666:609–625, September 2007.